Chemical Engineering Journal 527 (2026) 171521

Contents lists available at ScienceDirect

Chemical Engineering Journal

journal homepage: www.elsevier.com/locate/cej

Coalescent 2D heterostructure for high-efficient surface-enhanced Raman scattering and electrochemical sensing

Muhammad H. Nawaz [a], S. Santhoshkumar [b], Thi H. Ho [c,d], Balamurugan Arumugam [b], Mohamed Gamal Mohamed [e], Tuan V. Vu [c,d], Yousra.M. Nabil [e], Mohammed G. Kotp [e], Li-Wei Tu [a], Hung-Duen Yang [a], Ahmed F.M. EL-Mahdy [e], Shiu-Ming Huang [a], Po-Ling Chang [b], Trung Nguyen-Thoi [c,d], Shiao-Wei Kuo [e], Wei-Lung Tseng [b], Kin-Man Yu [a], Feng-Chuan Chuang [a,f,g,h,*], Phuong V. Pham [a,**]

[a] *Department of Physics, National Sun Yat-sen University, Kaohsiung, 80424, Taiwan*
[b] *Department of Chemistry, National Sun Yat-sen University, Kaohsiung, 80424, Taiwan*
[c] *Laboratory for Computational Physics, Institute for Computational Science and Artificial Intelligence, Van Lang University, Ho Chi Minh, 70000, Viet Nam*
[d] *Faculty of Mechanical - Electrical and Computer Engineering, School of Technology, Van Lang University, Ho Chi Minh, 70000, Viet Nam*
[e] *Department of Materials and Optoelectronic Science, National Sun Yat-sen University, Kaohsiung, 80424, Taiwan*
[f] *Department of Physics, National Tsing Hua University, Hsinchu, 30013, Taiwan*
[g] *Physics Division, National Center for Theoretical Sciences, Hsinchu, 30013, Taiwan*
[h] *Center for Theoretical and Computational Physics, National Sun Yat-sen University, Kaohsiung, 80424, Taiwan*

ARTICLE INFO

Keywords:
CuO@rGO/ITO
Coalescent 2D Heterostructure
Surface-enhanced Raman scattering (SERS)
Electrochemical sensing (ECS)

ABSTRACT

Surface-enhanced Raman scattering (SERS) and electrochemical sensing (ECS) are integrated components of modern and smart multifunctional electronic systems, but there are still plenty of rooms in mechanisms and fabrication strategies that need to be optimized. Herein, we report a coalescent 2D heterostructures to enhance electrocatalytic activity, sensitivity, and selectivity, made up of coalescent CuO@rGO on indium tin oxide, which serves as a dual-mode sensing platform delivering sheet resistance of 10.3 Ω/sq., transparency of 85.4 %, carrier mobility of 2.7×10^4 $cm^2/V \cdot s$, and work function of 2.2 eV. This interface enables a SERS enhancement factor of 9.62×10^6 by facilitating methylene blue detection efficacy of 1×10^{-9} M as a Raman reporter. For ECS, redox-active hydroquinone (HQ) and acetaminophen (ACP) perceive higher linearity compared with single 2D materials or metal oxide and exhibit exceptional limit of detection and sensitivity of 4.7 nM (1.7740 $\mu A\ \mu M^{-1}\ cm^{-2}$) for HQ and 6.3 nM (0.9037 $\mu A\ \mu M^{-1}\ cm^{-2}$) for ACP and applied in real tap water sample detection. This work highlights the capacity of rationally engineered 2D heterostructures for futuristic, high-performance, miniaturized, and multifunctional sensing technologies.

1. Introduction

Pursuit of rigid, durable, and solution-processable conductive electrodes has been a key research objective in the evolution of semiconducting circuits across several scientific fields, including smart textiles, transportation systems, medical instruments, OLED displays, touch screens, SERS, ECS, and modern wearable energy storage systems [1]. For the advancement of neoteric electrodes in contemporary technologies, achieving excellent electrical conductivity is essential [2]. These electrodes are often constructed using carbon-based materials, metals, and conductive polymers [3]. The incorporation of coalescent 2D heterostructures with these materials at the nanoscale enhances electrical conductivity, mechanical strength, device longevity, and overall performance [4,5]. Flatlands of metal oxides have been extensively studied in previous reports, with one of the emerging materials being copper oxide (CuO) [6]. CuO, a narrow bandgap p-type semiconductor, exhibits high electrical conductivity, thermal stability, and catalytic activity, playing a vital role in optoelectronics, power retention, electrocatalysis, antimicrobial coatings, and sensing applications [7]. However, its low oxidation resistance and nanoscale aggregation

---

* Corresponding author at: Department of Physics, National Sun Yat-sen University, Kaohsiung, 80424, Taiwan.
** Corresponding author.
E-mail addresses: fchuang@mail.nsysu.edu.tw (F.-C. Chuang), phuongpham@mail.nsysu.edu.tw (P.V. Pham).

https://doi.org/10.1016/j.cej.2025.171521
Received 16 July 2025; Received in revised form 16 November 2025; Accepted 1 December 2025

hinder its long-term stability and conductivity [8]. These challenges can be addressed by engineering CuO into a coalescent 2D heterostructures, which promotes efficient charge transport, structural stability, and surface reactivity [9].

Coalescent 2D heterostructures aided electrodes, particularly those anchored on metals integrated with the broad family of graphene [3] offer numerous benefits, including low sheet resistance, high surface area, chemical redox activity, thermal stability, and exceptional mechanical integrity [10]. Among these, reduced graphene oxide (rGO) has emerged as a promising material for enhancing the performance of CuO-related heterostructures [11]. The presence of functional groups in rGO provides ideal anchoring sites for CuO nanoparticles, enabling them to be uniformly dispersed and enhancing the interaction between constituents [12]. This coalescence improves the heterostructure's electrical conductivity, mechanical stability, chemical resilience, and dielectric strength [13]. Coalescent CuO@rGO demonstrated efficacy in traditional SERS and ECS, owing to their strong interfacial adhesion, efficient charge transfer, surface activity, and reactivity. In the SERS model, the enlarged interfacial area and facilitated charge delocalization intensify the Raman signal across a broad range of molecules [14]. Concurrently, coalescent CuO@rGO interface exhibits ultrahigh sensitivity and ultralow detection limits for trace analytes in ECS modalities due to its excellent electrical conductivity, making it a compelling candidate for ecological screening and analytical sensing platforms [15]. However, CuO@rGO heterostructures suffer from signal fluctuations and reduced stability during prolonged operation, limiting their reliability in SERS and ECS applications [16].

Coalescent 2D heterostructures (CuO@GO/ITO) offer a promising multifunctional platform for the deployment of SERS and ECS, owing to their high electrical conductance, rapid surface reactivity, strong adhesion, efficient charge transfer capability, optical transparency, and mechanical resilience [17]. In the context of SERS, coalescent 2D heterostructures (CuO@GO/ITO) interfaces provide a highly sensitive and reproducible platform for molecular detection, enabling synergistic enhancement of both chemical effects and the local electromagnetic field [18]. This is driven by charge transfer processes resulting from integrated of CuO, GO, and ITO components, collectively leading to strong Raman signal amplification [19]. In addition to ECS, coalescent 2D heterostructures (CuO@GO/ITO) exhibits rapid kinetic response and high detection sensitivity toward a wide range of analytes, enabling its use in chemical inspection and environmental monitoring through electrochemical transduction mechanisms [20]. The development of conventional SERS technology is hindered by inherent limitations, including poor sensitivity, non-reproducible performance, and signal instability primarily due to plasmonic nanoparticle aggregation and inefficient electromagnetic field enhancement at the substrate interface [21]. To mitigate these issues, semiconductor materials such as metal oxides, TMDs, graphene, and MXenes have been used to enhance SERS signals, owing to their high chemical stability, good biocompatibility, and ability to facilitate charge transfer (CT) interactions [22]. Herein, we propose coalescent 2D heterostructures (CuO@GO/ITO) proposed as a stable alternative, leveraging their ability to locally enhance electromagnetic charge transfer fields and stabilize signal output, thereby enabling efficient and high-performance SERS activity [23]. Similarly, prior ECS technologies face challenges such as low electron transfer rates, reduced selectivity, and inadequate sensitivity at low analyte concentrations, primarily due to attenuated active sites and conductivity [24]. The coalescent 2D heterostructures circumvents these limitations by improving electrical conductivity and surface area, as well as providing more active sites, such as oxygen vacancies and surface hydroxyl groups, which enhance sensitivity and selectivity in electrochemical sensing [25]. Prior research on 2D materials for SERS and ECS has mainly focused on single component semiconductors, graphene derivatives, or plasmonic nanoparticles [26]. While these platforms had localized Raman enhancement or moderated electrochemical sensitivity, the platforms typically had poor reproducibility, unstable signals, nanostructure aggregation, and limited multifunctionality [27]. Furthermore, conventional 2D structures basically lacked the combined attributes of optical transparency, low sheet resistance, and long-term stability that restricted their integration into scalable multifunctional devices [28].

This work focuses on the successful synthesis of coalescent 2D heterostructures (CuO@GO/ITO) via a hydrothermal approach, resulting in commendable conductivity (10.3 Ω/sq), transparency (85.4 %), and enhanced resistance to oxidative degradation, making it suitable for operation in harsh ambient environments. Density functional theory (DFT) and ab initio molecular dynamics (AIMD) calculations also confirmed enhanced water adsorption (−0.73 to −0.13 eV), strong binding of the coalescent 2D heterostructure CuO@GO/ITO (−5.54 eV), and stable charge transfer. The innovative SERS performance of the coalescent 2D heterostructure CuO@rGO/ITO delivers a substantial enhancement factor (9.62×10^6 at 1×10^{-9} M), along with excellent signal reproducibility (RSD: 5–10 %). In the case of advanced ECS, the coalescent 2D heterostructure demonstrates high sensitivity and selectivity for HQ (LOD: 4.7 nM, sensitivity: 1.7740 μA μM^{-1} cm^{-2}) and ACP (LOD: 6.3 nM, sensitivity: 0.9037 μA μM^{-1} cm^{-2}). In comparison to previous SERS and ECS platforms, our coalescent 2D heterostructure CuO@rGO/ITO aided SERS and ECS offers significantly higher sensitivity, signal stability, and multifunctionality for accurate detection under ambient conditions at ultralow analyte concentrations. This research opens new avenues for the use of coalescent 2D heterostructures (CuO@GO/ITO) in nanomaterial and electronics engineering technology development, with excellent potential for future applications in SERS and ECS-related systems.

2. Results and discussion

To synthesize a superior coalescent 2D heterostructures (CuO@GO/ITO), GO and CuO are added to deionized water (DI water) and subjected to ultrasonic agitation for 30 min. In an ultrasonic bath, the acoustic cavitation phenomenon induced by swift pressure oscillations leads to the formation and collapse of bubbles within milliseconds. This collapse generates localized temperatures of up to 5000 °C and pressures of thousands of bars, facilitating sonochemical reactions for the dispersion of GO and CuO solutions [29]. The resulting solutions undergo stirring and centrifugation, then are fused with different concentrations, consisting of nanoflake sheets of hydrophilic GO decorated with superparamagnetic CuO nanoparticles. CuO nanoparticles are effectively distributed on GO and introduce oxygen-containing functional groups, which suppress agglomeration, strengthen interactions with nanomaterial layers for improved stability, and promote uniform dispersion (Supporting Information Fig. S1), subsequently coated onto substrates using a spin coater. Thin films of coalescent CuO@GO were dried at room temperature and annealed in a CVD tube (see in Experimental Section). Heating the thin films in an Ar gas environment removes oxygen-containing functional groups from the GO and CuO layers, which plays an important role in increasing the electrical conductivity of the thin film. Finally, a coalescent 2D heterostructures of rGO supported CuO was deposited on bare glass and ITO-coated glass, where oxygenated functional groups present in the nanomaterials (CuO and rGO) contribute to the adhesion of CuO@rGO on ITO (Fig. 1a). However, despite ITO's wide applicability, it suffers from intrinsic brittleness, rendering it susceptible to mechanical fatigue and chemical degradation, and environmental exposure may eventually lead to crack formation. In contrast, coalescent 2D heterostructures (CuO@GO/ITO) are more mechanically strong and environmentally stable, imparting greater resistance against oxidative degradation and corrosion by air, which are critical characteristics for the stable operation of heterostructures in SERS and ECS applications [30].

For validating and interpreting our experimental findings, DFT and AIMD calculations were performed to investigate the effects of CuO incorporation into GO and its subsequent integration with ITO substrate.

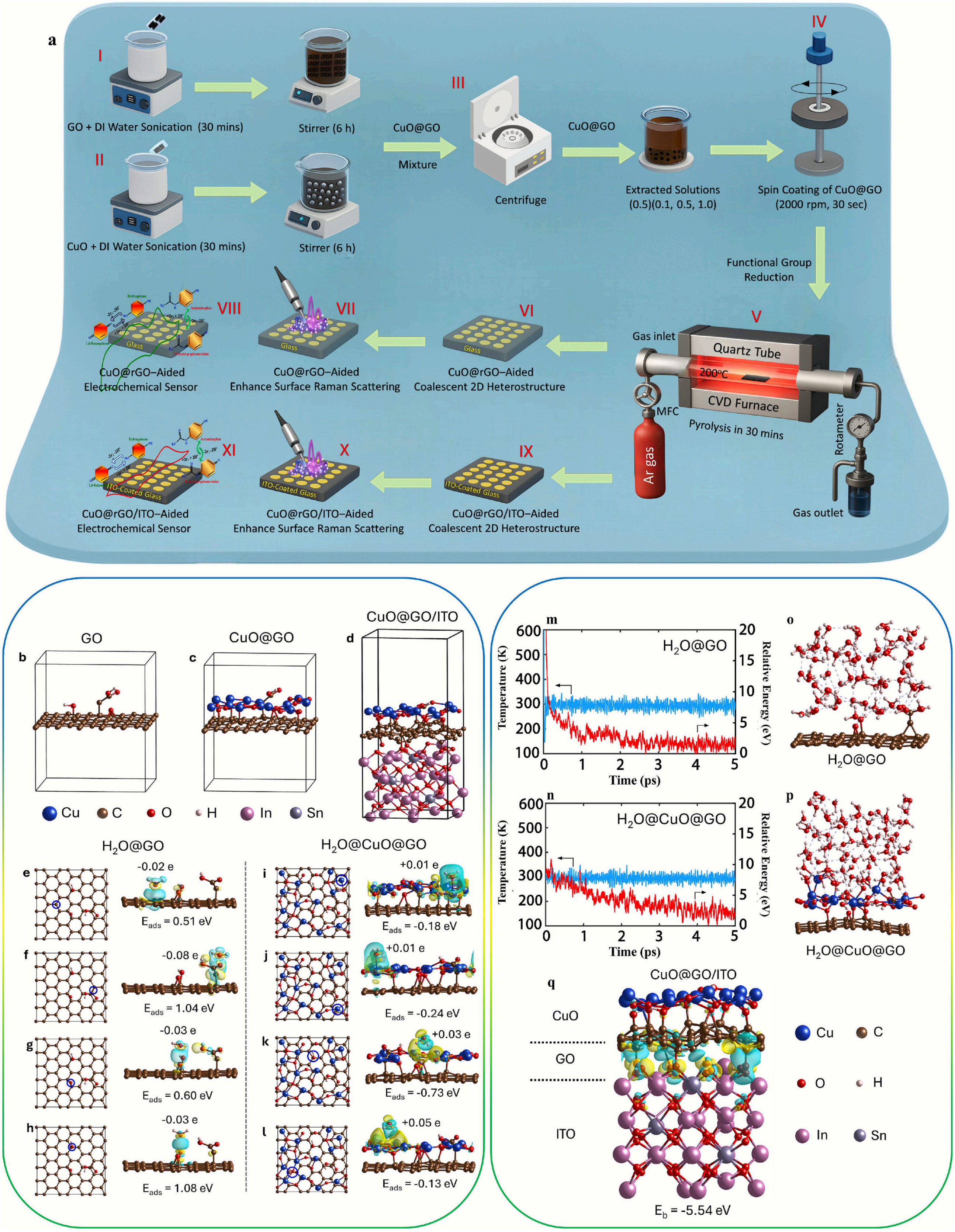

(caption on next page)

Fig. 1. Experimental and computational study of advanced coalescent 2D heterostructure. a) 3D schematic display process for synthesis of CuO nanoparticles, GO nanoflake sheets, CuO@rGO/coated glass and CuO@rGO/ITO-coated glass aided transparent electrodes. Supercells of b) GO, c) CuO@GO, and d, CuO@GO/ITO used in DFT calculations. Blue, brown, red, white, pink, and grey spheres represent Cu, C, O, H, In, and Sn, respectively. Relaxed structure with adsorption energy E_{ads}, differential charge density, and Bader charge density transfer of H_2O molecule on GO and coalescent CuO@GO surfaces at various adsorption sites. Panels e-h) illustrate adsorption sites on C atom, hydroxyl, epoxide, and carbonyl functional groups of GO. Panels i-l depict adsorption sites on Cu and O atoms of CuO@GO. In charge density plots, yellow and blue isosurfaces represent charge accumulation and depletion. Positive and negative values of charge transfer indicate charge gain and loss of H_2O molecules, respectively. m, n) Temperature (blue) and relative energy (red) during water adsorption on GO and coalescent CuO@GO surface over time. o, p) Snapshot of adsorption process of water on surfaces at last step of MD simulations. Blue, brown, red and white spheres represent Cu, C, O, and H atoms, respectively. q) Differential charge density at coalescent 2D heterostructures (CuO@GO/ITO) interface with binding energy E_b for SERS and ECS. Yellow and blue isosurfaces illustrate regions of charge accumulation and depletion, emphasizing chemical bonding between coalescent CuO@GO and ITO. Spheres in blue, brown, red, white, pink, and grey represent Cu, C, O, H, In, and Sn atoms, respectively.

These theoretical investigations are crucial for understanding how the interfacial chemistry and surface interaction mechanisms translate into the improved sensing performance of the coalescent CuO@GO. To simulate the system, we constructed three representative unit-cell models: GO, CuO@GO, and advanced coalescent 2D heterostructures (CuO@GO/ITO) (Fig. 1b–d). To assess the water solubility of GO and CuO@GO, the adsorption energies (E_{ads}) of a single H_2O molecule on the their surfaces were first calculated, since solubility strongly influenced by water adsorption and hydration, which are a key determinant of dispersion and film stability [23]. The relaxed structures of H_2O on both GO and coalescent CuO@GO surfaces, along with their adsorption energies, differential charge densities, and Bader charge transfers were computed (Fig. 1e–l). Here, negative E_{ads} values correspond to favorable adsorption, whereas positive values indicate unfavorable adsorption. On GO surface, possible adsorption sites were examined (Fig. 1e–h), including basal carbon atoms as well as hydroxyl, epoxide, and carbonyl groups. All of these sites exhibited unfavorable energetics, with positive adsorption energies between 0.51 and 1.08 eV. The weak interaction between the H_2O molecule and the GO surface is attributed to the hydrophilic nature of the graphene basal plane [24], and the presence of oxygen-containing functional groups does not significantly enhance water adsorption. This aligns with the experimental observation that GO dispersions are unstable and prone to aggregation, leading to difficulties in forming stable and homogeneous films. Conversely, the coalescent CuO@GO surface exhibited opposite behavior, with negative energy values from -0.73 to -0.13 eV, indicating favorable water adsorption (Fig. 1i–l). Enhanced interactions between H_2O and the coalescent CuO@GO are attributed to the presence of unsaturated Cu and O atoms at the CuO surface, which act as chemically active adsorption sites [25]. These results correlate directly with the experimentally observed improvement in water solubility, which promotes uniform dispersion and enables the successful fabrication of uniform CuO@GO/ITO films.

To gain a deeper insight into how H_2O interacts with the surfaces in relation to adsorption behavior and water solubility, we conducted analyses on differential charge density and Bader charge transfer. In charge density plots, yellow isosurfaces indicate regions of charge accumulation, while blue isosurfaces represent regions of charge depletion. For the GO surface, differential charge density analysis reveals that H_2O forms only weak and non-bonding interactions, with evident charge depletion between the molecule and the adsorption site, resulting in unfavorable adsorption with positive E_{ads}. Bader charge transfer analysis further exhibited negative values, suggesting that the H_2O molecule loses charge upon adsorption. This charge loss weakens its interactions with the GO surface, reinforcing the unfavorable adsorption energies observed. In contrast, the coalescent CuO@GO surface exhibits large charge accumulation and favorable charge transfer toward H_2O, consistent with stronger binding and highlighting the role of CuO in enhancing water solubility.

To more closely mimic aqueous environments and assess thermal stability, we performed AIMD simulations at room temperature (300 K) for 5 ps. Temperature and relative energy over a 5 ps period are illustrated in (Fig. 1m, n). For both surfaces, temperature remained stable around 300 K, and relative energy fluctuations converged, indicating thermal stability during simulations. On GO surface, water molecules remained poorly organized and separated (~3.32 Å average separation, Fig. 1o), consistent with the experimentally poor water solubility and dispersion of GO. Consequently, water molecules are loosely organized above the GO surface, resulting in positive E_{ads}. In contrast, water molecules were strongly adsorbed and ordered around CuO clusters on CuO@GO (Fig. 1p), producing a robust hydration shell. This absorption also causes slight bending of the CuO@GO film, reflecting strong interactions between H_2O and the surface. The presence of CuO clusters provided abundant active sites for water adsorption, resulting in stronger binding and negative E_{ads} values compared to GO. Such behavior explains the experimentally observed improvement in water solubility, uniform dispersion, and the successful formation of stable coalescent CuO@GO. In summary, the combination of DFT and AIMD simulations demonstrates that the coalescent CuO@GO possesses a much higher affinity for water molecules than GO, consistent with experimental results showing enhanced water solubility and stability in the coalescent heterostructure.

To examine the adhesion and the interfacial bonding capability of the coalescent CuO@GO with ITO, additional DFT calculations were carried out to evaluate the binding energy (E_b). The interface exhibited a large negative binding energy E_b of -5.54 eV (Fig. 1q), confirming that the bonding is energetically favorable. Differential charge density analysis further revealed clear charge redistribution across the interface, signifying strong chemical interactions. Specifically, strong charge accumulation was observed between oxygen atoms in ITO and carbon atoms in coalescent CuO@GO, indicating the formation of robust O—C chemical bonds. These bonding interactions are critical for stabilizing the CuO@GO/ITO heterostructure and are consistent with the experimental findings of excellent electrical and optical properties.

The dispersion behaviors of CuO, GO and their coalescent CuO@GO in DI-water were systematically examined for a series of concentrations (Fig. 2a). A laser light shining across solution bottles provides visual assistance, clearly indicating suspended materials. UV–Visible (λ = 200nm–800 nm) spectra of solutions were employed to probe electronic structure and optical response of materials by revealing specific wavelengths at which a compound absorbs light, indicating the presence of certain functional chromophores. Band gap of a material directly correlating with its color variation is observed in CuO, GO, and coalescent CuO@GO coated films on basic glass and ITO-coated glass before heating and this serves as a pivotal indicator of their structural and compositional differences (Fig. 2b, c). To further elucidate UV–visible spectrum of CuO exhibits an absorption peak at 286 nm and a high light transmission (93.4 %), GO peak at 270 nm (80.4 %). Coalescence solution of CuO with GO exhibited progressively redshift absorption for CuO@GO (0.5, 0.1) peaks at 270 nm (89.4 %), CuO@GO (0.5, 0.5) peaks at 273 nm (85.9 %) and CuO@GO (0.5, 1.0) peaks at 278 nm (83.7 %) (Fig. 2d, e). Decline in absorption peak, and light transmission due to accumulation of GO into different concentration solutions, cause of decrease in band gap due to redox reaction between CuO and GO (i.e. CuO + GO→Cu + rGO + H_2O), restore π-conjugated network (sp^2 bonding), enhances conductivity and light absorbance. When a redox reaction occurs, it introduces new energy levels that facilitate more electronic transitions, are key attributes for optimal SERS and ECS performance. These new energy levels facilitate electron transitions,

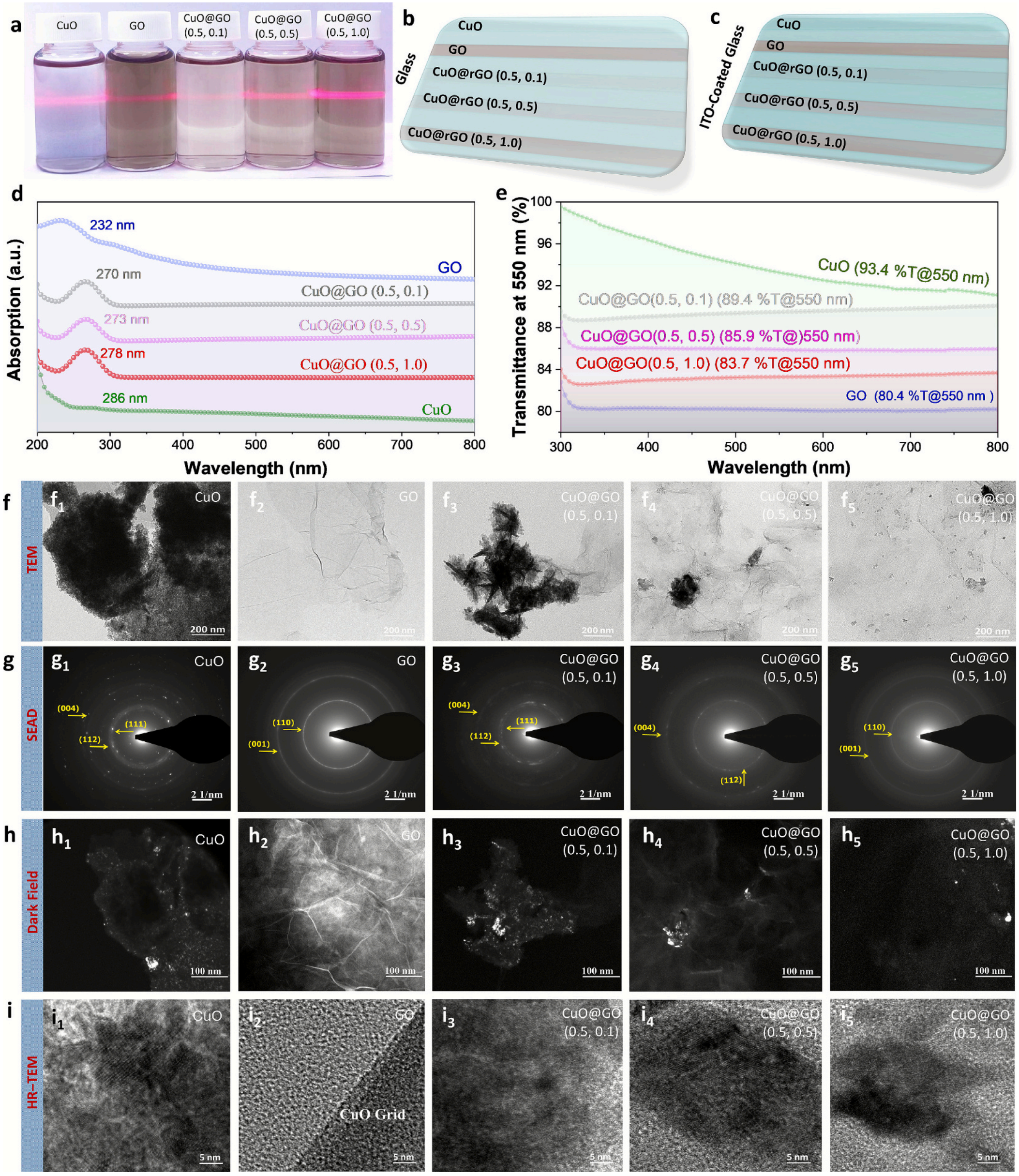

Fig. 2. Optical and structural characterization. a) Digital photograph of CuO, GO and CuO@GO dispersion in DI water under laser light illumination. b, c) Distinct colors variation of CuO, GO, coalescent CuO@GO on basic glass and ITO-coated glass substrates used for contact angle measurement. d, e) UV analysis and light transmission through solutions. f) TEM images, g) SEAD patterns, h) Dark field TEM images and i) HRTEM images of CuO, GO, coalescent CuO@GO.

effectively reducing energy difference between valence band and conduction band. These visual distinctions not only facilitate identification of heterostructures but also correlate with their wettability properties, as evidenced by adhesion angle measurements (Supporting Information Fig. S3) [34].

High-resolution TEM imaging analyses were carried out to study vast microstructures, defects, crystallography, chemical composition, and nanomorphology of GO nanoflakes, CuO, and coalescent CuO@GO on a Cu grid before annealing (200 °C in an Ar gas flow). CuO and GO exhibit perfect dispersion during exfoliation (Fig. 2f$_1$, f$_2$), which reflects high structural integrity and no nanoscale agglomeration. Beyond dispersion behavior, CuO-like nanospheres exhibit a cupric phase crystalline structure with a lattice fringe spacing of 0.24 nm link to (111) plane in the high resolution image and diffraction rings corresponding to (111), (112), and (004) planes of the cupric phase in the SAED (Fig. 2g$_1$) [35]. In addition, GO is present in the form of nanosheets that possess a folded silk veil-like morphology and ripple, reflecting its semicrystalline nature, and diffuse rings (110), (001) reported (Fig. 2g$_2$), typical consists of graphitic (sp^2) regions interspersed with oxidized (sp^3) frameworks. These TEM analyses show that two morphologies exist: spherical CuO nanospheres tightly bound on the surface of wrinkled GO sheets by van der Waals forces. Structural stability of coalescent CuO@GO improves with higher GO composition, forming a more networked framework that enhances material stability and dispersion of CuO. At low content CuO@GO (0.5,0.1), GO provides limited availability of functional groups for CuO anchoring, leading to a loosely assembled and poorly integrated heterostructure. As GO content increases for CuO@GO (0.5,0.5), CuO dispersion and interfacial interaction are enhanced by attraction force, resulting in more CuO-O-C bonds wrapping. For CuO@GO (0.5,1.0), GO create more structural amalgamation and open continuous interfacial electron transportation within coalescent CuO@GO films (Fig. 2f$_3$-f$_5$). SAED diffraction patterns of heterostructures reveal that the distinct crystalline pattern of CuO's change into a less crystalline with increasing content of GO into coalescent

CuO@GO composition (Fig. 2g_3-g_5). The diffraction can be indexed as (110), (111) for CuO@GO (0.5,0.1), (110), (112) for CuO@GO (0.5, 0.5), and (004), (110) for CuO@GO (0.5, 1.0) [36]. These phases trend in dark field microscopy of CuO, GO, and CuO@GO heterostructures, CuO and GO regions appear dark on a dark background due to electron transmission, which outlines their shape, mass density and distribution (Fig. 2h_1-h_5). To resolve heterointerfaces high-resolution images obtained due to wave nature of electrons, clearly exhibit CuO lattice fringes (Fig. 2i_1), GO semicrystalline phase (Fig. 2i_2), and intercalation of coalescent CuO@GO films at nanoscale (Fig. 2i_3-i_5) [37].

Uniform nanostructural morphological analysis is further supported by Fourier transform infrared (FTIR) spectroscopy, which informs surface chemistry and functional group topography of coalescent 2D heterostructures. FTIR spectra of GO, CuO and CuO@rGO depict functional groups on surface of materials. Upon heating coalescent CuO@GO under Ar gas flow, a reduction in the peak intensity was observed due to

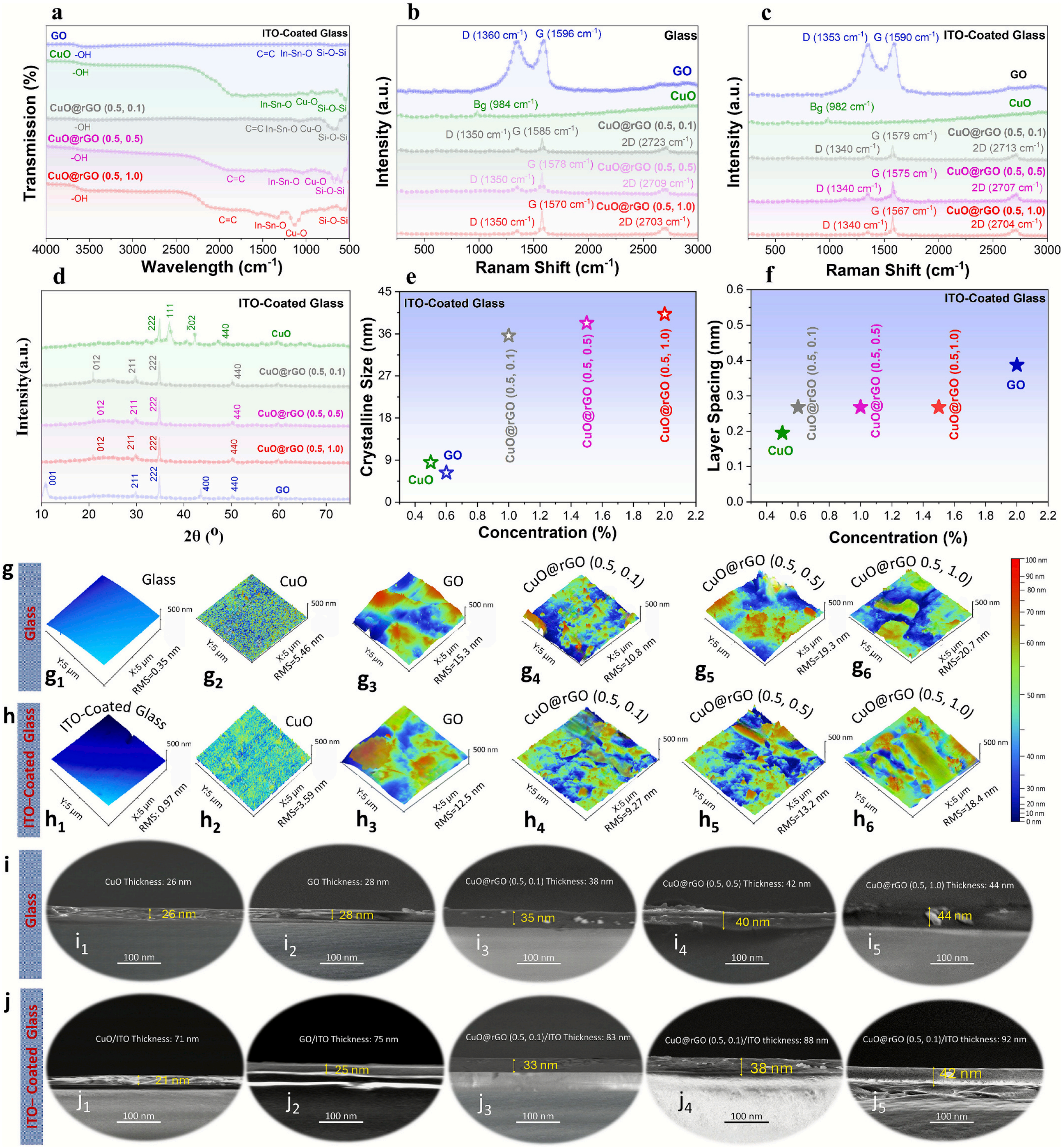

Fig. 3. Functional structure assessment of coalescent 2D heterostructure. a) FTIR spectra showing functional group identification b, c) Raman spectrum for defect density and chemical interaction d–f) XRD analysis for crystalline, particle size and layer spacing. g, h) AFM images of surface topography and root mean square roughness (cross section area: 5 × 5 μm^2) i, j) SEM images depict sheet thickness of CuO, GO, and coalescent CuO@rGO 2D heterostructures.

removal of functional groups on sphere of CuO and GO nanoflakes sheet that hinder the charge mobility, thereby enhanced electrical conductivity of CuO@rGO films. CuO, GO and coalescent CuO@rGO films coating on ITO-coated glass, bare glass (Fig. 3a), and powder (KBr pellets samples) evidenced (Supporting Information Fig. S5a, b) exhibited alkane hydroxyl (—OH), alkene aromatic (C═C), and metal oxide (Cu—O), Indium tin oxide (In—Sn—O) and silicon oxide (Si—O—Si) functional groups. These functional groups facilitate interfacial chemical bonding (covalent) of coalescence layers with supporting substrate, leading to an improved film adhesion, mechanical integrity, and environmental stability.

The phase characterization of GO sample exhibits two prominent Raman bands at (1360 cm^{-1}, 1596 cm^{-1}) on glass, (1353 cm^{-1}, 1590 cm^{-1}) on ITO-coated glass, corresponding to the GO D band (defect of material) and G-band (quality of material) (Fig. 3b, c). These peak positions are consistent with previous studies [38] and the calculated I_D/I_G ratio is 0.852, 0.850, respectively, which confirms nanoflake sheets structure of GO. This ratio indicates the presence of a significant amount of disordered hexagonal carbon sp^2 networks within the GO lattice. Additionally, CuO NPs display characteristic Raman bands at 984 cm^{-1} (B_g) for the film on glass, and 982 cm^{-1} (B_g) for the film on ITO-coated glass, confirming that CuO crystallizes in a monoclinic structure [39]. Examining Raman spectra of coalescent CuO@rGO samples with various composition ratios of (0.5, 0.1), (0.5, 0.5), (0.5, 1.0) reveals several notable features in the D, G and 2G bands. Firstly, there is a significant increase in intensities of G and 2D bands, indicating a high density of sp^2 carbon networks within lattice due to rGO content, which support delocalized π-electron networks. This enhancement is beneficial for electrical and thermal transport properties, such as conductivity, due to the presence of delocalized π-electron networks in sp^2 carbons. Secondly, the intensity of 2D band increases linearly with the rGO content in heterostructures. Raman spectra of coalescent CuO@rGO (200 °C) at ratios of (0.5, 0.1), (0.5, 0.5), (0.5, 1.0) exhibits I_D/I_G intensity ratios (0.851, 0.855, 0.859) for glass and (0.848, 0.852, 0.855) for ITO-coated glass. Compared to Raman band positions of pure GO, a significant downward shift is observed in D and G bands. This shift is due to a reduction process, which facilitates removal of hydroxyl groups and initiates formation of CuO to Cu and GO to rGO layers. Furthermore, presence of 2D band at (2723 cm^{-1}, 2709 cm^{-1}, 2703 cm^{-1}) for glass, (2713 cm^{-1}, 2707 cm^{-1}, 2704 cm^{-1}) for ITO-coated glass, along with its intensity, provides unequivocal evidence for the formation of rGO layers (multiple layers) during the reduction process. Raman bands associated with CuO NPs, such as those at 982 cm^{-1} (B_g) for glass, 984 cm^{-1} (B_g) for ITO-coated glass, are not observed in coalescent CuO@rGO. This absence due to weak intensity of CuO that become not observable when diluted and high scattering efficiency of sp^2 hybridized carbons [40].

To further clarify structural ordering and phase features of synthesized materials, X-ray diffraction (XRD) measurement was employed as a complementary crystallographic analysis technique. XRD patterns of glass and ITO-coated glass reveal the amorphous nature of the glass substrate and the polycrystalline structure of the ITO-coated film on glass (Supporting Information Fig. S6a). For films deposited on ITO-coated glass, the diffraction pattern of CuO reveals a monoclinic phase with diffraction peaks from (222), (111) and ($\bar{2}$02) planes. In contrast, the diffraction pattern of the GO thin film exhibits an semicrystalline phase, with broad diffraction peaks indexed to the (001), (211), (222) and (400) planes. The coalescent CuO@rGO have nanocrystalline phase exhibits diffraction peaks from (012), (222) and (211) planes. The heterostructures exhibit less crystalline structural phase, as suggested by the decreased intensity of sharp diffraction peaks due to GO. Moreover, peaks corresponding to (222) and (440) plane identified presence of Sn in ITO-coated layer on glass, where it enhanced electrical conductivity (Fig. 3d) [41]. The size of nanomaterials (D) and layers interplanar spacing (d) were calculated by taking diffraction peaks at angel 2θ is equal to 34.8° for CuO, 10.8° for GO, and 35.2° for coalescent CuO@rGO. The sizes of CuO particle (D = 18.1 nm), GO nanosheets (D = 8.4 nm), CuO@rGO (0.5, 0.1) (D = 20.2 nm), CuO@rGO (0.5, 0.5) (D = 20.5 nm), and CuO@rGO (0.5, 1.0) (D = 20.7 nm) were determined. In coalescent CuO@rGO value of D vary at same angle due to shift of crystalline peak sharpness to broad width (Fig. 3e) [42]. Moreover, d-spacing between layers of CuO (d = 0.257 nm), GO (d = 0.818 nm), CuO@rGO (0.5, 0.1), CuO@rGO (0.5, 0.5), and CuO@rGO (0.5, 1.0) is same (d = 0.255 nm), supporting consistent interlayer arrangement (Fig. 3f). For bare glass substrate, where X-ray diffraction results for CuO (2θ = 36.4°), GO (2θ = 11.6°), and coalescent CuO@rGO (2θ = 26.6°) (Supporting Information Fig. S6b–d). The surface energy (97.7 mJ/m^2) of ITO-coated glass (83.4 mJ/m^2) is typically higher than that of bare glass. This factor affects the wetting behavior of the heterostructure during deposition, leading to variations in layer spacing. Higher surface energy promotes better adhesion and spreading of heterostructure, potentially resulting in a more uniform layer and different interlayer spacing. However, the combination of the coalescent CuO@GO structure with a thickness range of 20.2–20.7 nm forms a single-layer coating on the substrates, positively impacting sheet dimensions (valuable for optical properties) and uniformity (critical for conductivity) [43].

Following the crystallographic evaluation, atomic force microscopy (AFM) was employed to gain valuable insights into the material's structural and surface properties by analyzing the topography, surface roughness, and morphology of CuO@rGO films on glass and ITO-coated glass substrates. AFM measurements were carried out on pristine glass, ITO-coated glass substrates along with thin films of CuO, GO, coalescent CuO@rGO grown on glass and ITO-coated glass, to investigate their physical properties with surface roughness (Fig. 3g, h). AFM reveals a smooth topography for bare glass and the presence of nanoscale roughness on ITO-coated glass. Such surface features of the ITO layer provide improved anchoring sites for the coalesced CuO@rGO nanostructures, leading to improved adhesion and improved interfacial stability compared to bare glass. After heat treatment and drying, CuO, GO, and CuO@rGO films exhibit significantly enhanced adhesion on the ITO surface due to its porous structure and higher interfacial interactions. In contrast, bare glass has a smooth, featureless surface with low anchoring capability and poor film attachment, as evidenced by higher surface roughness. All samples 3D AFM views revealed homogeneous spherical grains, nanoflakes sheets of films, and densely packed CuO particles on surface of GO. RMS roughness values were obtained for the different samples (Fig. 3$g_{1-}g_{6,}$ $h_{1-}h_{6}$) arise from differences in interfacial energy, nucleation density, and lattice compatibility between film–substrate. Layer examination revealed that higher GO concentrations enhanced the consistency and surface roughness of the CuO@rGO coating films. Bare glass has lower surface energy, leading to poorer wetting and adhesion. As a result, CuO@rGO layers tend to aggregate more randomly on glass, forming a rougher and less compact film. A significant change in root mean square (RMS) roughness was observed with the incorporation of GO. The high-performance CuO@rGO (0.5, 1.0) film on glass exhibited greater RMS roughness (20.7 nm) compared to the CuO@rGO (0.5, 1.0) film on ITO-coated glass, which showed an RMS roughness of 18.4 nm. The surface roughness of coalescent CuO@GO films deposited on ITO-coated glass exhibits a minimal value, indicating a low density of defects within the sheet, as further confirmed by focused ion beam analysis (Supporting Information Fig. S9) [44].

Surface morphology was also studied by SEM and the images reveal the absence of cracks, pores, or cavities for films on either of substrates, with smoothness observed for ITO-coated glass (Supporting Information Fig. S4a) [45]. Relative roughness measurements using AFM confirmed the lower surface roughness of ITO, thereby ensuring better film uniformity and stronger adhesion. A pure CuO coating exhibited spherical nanocrystalline structures, while GO formed smooth, defect-free nanosheets on both glass (Supporting Information Fig. S8a_1, b_1) and ITO-coated glass (Supporting Information Fig. S8a_2, b_2). EDS analysis exhibited a uniform distribution of CuO and GO, indicating a well coalesced CuO@rGO/ITO 2D heterostructure [46]. The film thickness increased with the addition of GO to CuO; annealing at 200 °C in an Ar atmosphere enhanced surface uniformity and reduced crack formation (Supporting Information Fig. S8a$_3$-a$_5$, b$_3$-b$_5$). Further explore structural features, CuO sheet thicknesses of GO, CuO, and coalescent CuO@rGO were examined by cross-sectional SEM, and the findings showed greater values on glass than on ITO-coated glass, which was attributed to differences in surface roughness (Fig. 3i, j). Thickness is of significance for material property optimization, e.g., conductivity, surface morphology, and roughness. As the amount of GO in CuO increases, the thickness of the coalescent CuO@rGO also increases. The brittle layer of ITO on glass was observed by SEM, revealing a thickness of 50 nm on the glass substrate (Supporting Information Fig. S4b). The layer thicknesses of CuO, GO, and CuO@GO at various ratios on glass and ITO-coated glass are indicated on the SEM images shown in (Fig. 3i$_1$-i$_5$, j$_{1-}$j$_5$). In comparison to other layers, CuO@rGO (0.5, 1.0) layers have large thickness in terms of conductivity and coverage, specifically for glass (44 nm) and ITO-coated glass (42 nm). These layer thicknesses ensure effective mechanical stability and strong adhesion, achieving paradigm balance between interfacial resistance and carrier mobility across the film-substrate interface [47].

The enhanced performance of CuO@rGO films on ITO-coated glass arises from the synergistic combination of CuO (intrinsic electrical conductivity 1×10^{-3} S/cm) [48] with rGO (excellent electron mobility 26cm^2/Vs) [49] on the ITO film, which provides a stable, low-resistance

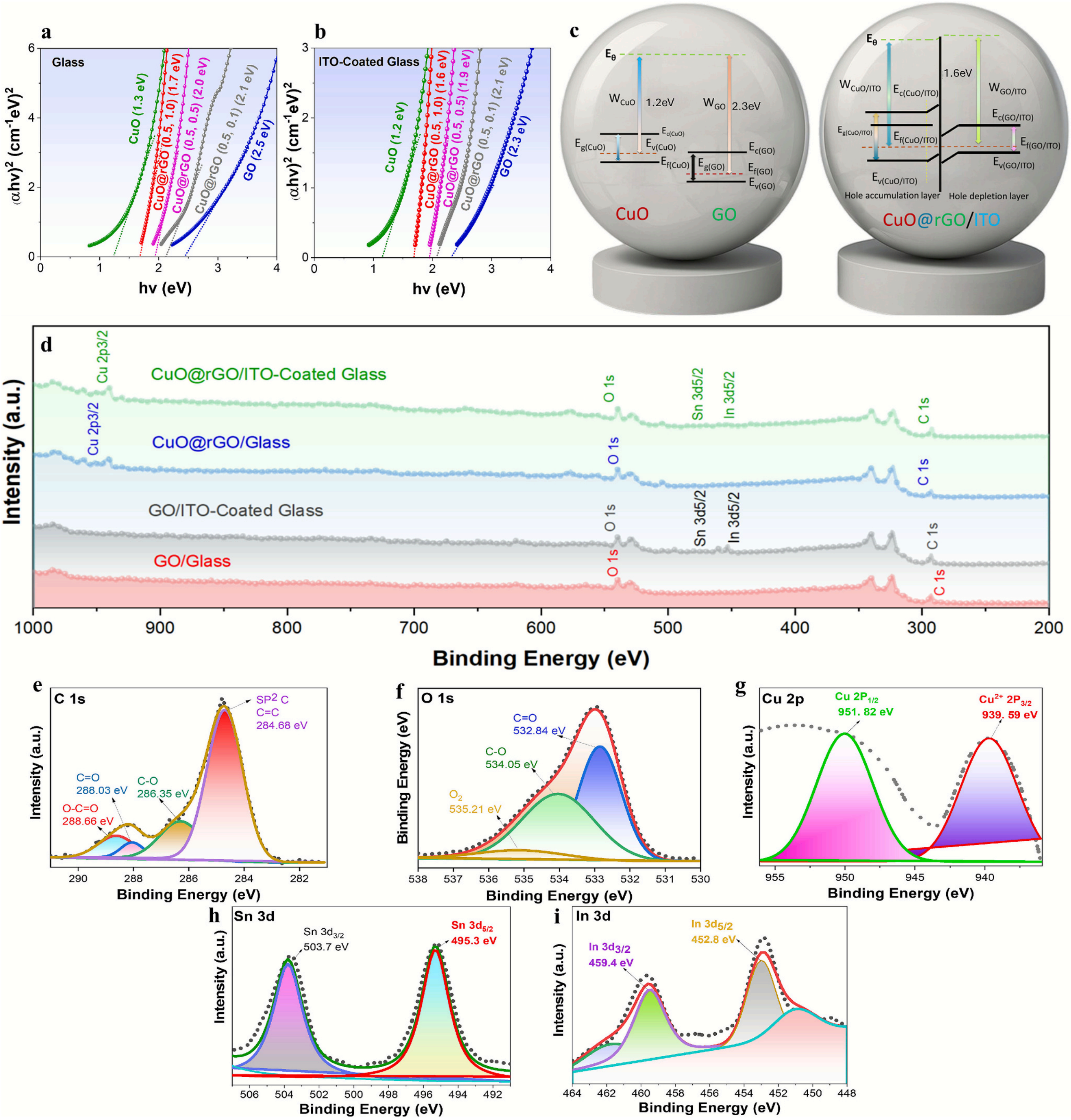

Fig. 4. Band gap influence by surface composition. a, b) Tauc's plots graph use to estimate the band gap of CuO, GO and coalescent CuO@rGO. c) Band diagram illustrates CuO@rGO/ITO heterostructures formation. d–i) XPS spectra showing binding energies and chemical states with deconvolution.

surface for the coalescent CuO@rGO. The rGO nanosheets act as conductive bridges between aligned CuO nanoparticles, facilitating efficient charge transfer. Higher sheet conductance is closely related to energy band structure, which significantly influences visible absorption. This relationship underscores the importance of energy bands in determining material's optical properties. Plots of the absorption coefficient versus photon energy enable the identification of the energy at which the material begins to absorb photons, indicating the transition of electrons from the valence band to the conduction band [50]. UV–Vis absorbance spectra (Supporting Information Fig. S7a) and band gaps of all prepared samples CuO, GO and coalescent CuO@rGO in solution were calculated by using Tauc's plots by subtracted the background absorption (Supporting Information Fig. S7b) [51,52]. Both CuO and GO films behave as insulators, with band gaps of 1.3 eV and 2.5 eV on glass, and 1.2 eV and 2.3 eV on ITO-coated glass, respectively. For CuO, the narrow band gap reflects its indirect transitions and defect states, while GO's band gap arises from π–π* transitions in its disordered sp^2/sp^3 carbon structure. With the incremental addition of GO into the CuO solution at different concentrations, the absorption edge shifted toward lower energy, indicating a systematic reduction in the band gap. GO contains abundant oxygen functional groups, and its partial reduction (rGO) introduces π-conjugated sp^2 domains. When GO is integrated with CuO nanoparticles, it interacts electronically, forming hybridized states at the CuO-GO interface. These interactions create localized states within the band gap of GO, effectively shrunk the band gap. The band gap of CuO@rGO (0.5, 0.1) is 2.2 eV on glass and 2.1 eV on ITO-coated glass, while CuO@rGO (0.5, 0.5) measures 2.0 eV on glass and 1.9 eV on ITO-coated glass. Eventually, the band gap for CuO@rGO (0.5, 1.0) is 1.7 eV on glass and 1.6 eV on ITO-coated glass (Fig. 4a, b) [53]. In a similar context, band gap diagram model of CuO, GO and superior coalescent 2D heterostructures (CuO@GO/ITO) are exhibit in (Fig. 4c).

A comprehensive investigation of the surface chemistry, elemental composition, and chemical states of CuO@rGO thin films was conducted using X-ray photoelectron spectroscopy (XPS). To probe the buried ITO layer and its interaction with the CuO@rGO film, we employed low-energy Ar^+ ion sputtering (1 kV, 1 μA) under ultra-high vacuum, enabling controlled surface removal and depth profiling to access the ITO interface. XPS analysis of the C 1 s, O 1 s, Cu 2p, Sn 3d, and In 3d core-level spectra was performed for GO/glass, GO/ITO-coated glass, CuO@rGO/glass, and the superior coalescent 2D heterostructures (CuO@GO/ITO-coated glass), providing valuable insights into their electronic structure and chemical environment (Fig. 4d). Deconvolution of C 1s spectrum from coalescent 2D heterostructures (CuO@GO//ITO), where (Fig. 4e) revealed a major peak at 284.68 eV, indicating sp^2 hybridized C═C bonding, along with additional peaks at 286.35 eV, 288.03 eV, and 288.66 eV, attributed to C─O, C═O, and O─C═O functional groups, respectively. The O 1s spectrum displayed peaks at 532.84 eV, 534.05 eV, and 535.21 eV, corresponding to C═O, C─O, and O_2, respectively, indicating the presence of oxygen-containing groups within the heterostructure (Fig. 4f) [54]. In the Cu 2p spectrum, peaks at 951.82 eV and 939.59 eV correspond to the $2p_{1/2}$ and $2p_{3/2}$ of Cu^{2+}, confirming the presence of CuO, (Fig. 4g). The Sn3d core level spectrum with the $3d_{5/2}$ binding energy at 495.3 eV corresponds to the Sn^{4+} state for SnO_2. Moreover, GO nanosheets provide electrical bridging among CuO nanoparticles and the ITO substrate, facilitating efficient charge transport across the heterostructure. The Sn $3d_{3/2}$ peak intensity of 503.7 eV guarantees the presence of SnO_2 in the ITO layer, which is revealed after sputtering. (Fig. 4h). In3d spectrum of CuO@rGO/ITO exhibited peaks at 452.8 eV for In $3d_{5/2}$ and 459.4 eV for In $3d_{3/2}$, corresponding to In_2O_3 (In^{3+}) (Fig. 4i). These XPS results revealed that GO nanosheets appear to be acting as conductive bridges, connecting CuO nanoparticles and ITO substrates by virtue of their rich π-conjugated sp^2 domains and oxygen-containing functional groups. Consequently, these bridges inject charges into the conductive ITO layer and promote charge transfer via π–d orbital interactions between CuO and rGO [55].

To extend our understanding of the optical response and electronic behavior of materials, photoluminescence (PL) spectroscopy was conducted on films on glass and ITO-coated glass substrates are exhibited in (Fig. 5a, b). Pure CuO exhibits two emission peaks at 360 nm and 720 nm associated with near-band-edge and deep-level emission. GO prominent peaks at 320 nm and 640 nm are attributed to recombination of electron-hole pairs in local state of sp^2 carbon clusters embedded within an sp3 matrix [56]. In coalescent CuO@rGO ratio (0.5,0.1: 0.5, 0.5: 0.5, 1.0), the PL peaks 360 nm and 720 nm intensity gradually elevated with GO content, reflecting enhanced radiative recombination CuO-GO interface. This enhancement is driven by improved charge carrier separation and reduced non-radiative recombination pathways due to π–d orbital interactions and better interfacial coupling with supporting materials [57].

Transmittance of light and sheet resistance in CuO, GO, and coalescent CuO@rGO (Fig. 5c, d) reveals a correlation between electrical conductivity and light transmittance in optical electrodes ((Supporting Information Fig. S7c, d). Transparent electrodes fabricated on glass and ITO glass, placed over the logo of Department of Physics, National Sun Yat-sen University, Taiwan, are visually presented in (Supporting Information Fig. S8e, f) demonstrating their transparency. Visible light transmittance of CuO, GO, and CuO-GO heterostructure films of varying ratios (Supporting Information Fig. S8e_1-e_6, f_1-f_6) [58,59]. In parallel, sheet resistance measurements reveal the electrical conductivity of the films, highlighting the trade-off between charge transport efficiency and transparency. CuO form irregular thin film due to less interfacial adhesion exhibits a transparency 95.8 % indicating that it allows a significant portion of light to pass, with a sheet resistance 1.02×10^5 Ω/sq. on glass (insulating material hinder charge movement), and 91.3 %T with a sheet resistance of 18.17 Ω/sq. on ITO-coated glass (ITO: conductive oxide with free carriers enhanced charge flow). GO produced uniform film due to π–π interactions, has a transparency of 82.9 % on glass with a sheet resistance of 3.98×10^6 Ω/sq., and 81.4 % on ITO-coated glass with a sheet resistance of 20.15 Ω/sq. The addition of GO leads to a reduction in sheet resistance. In case of mixture CuO@rGO (0.5, 0.1: 0.5, 0.5: 0.5, 0.1), transparency values are 89.7 %, 87.6 %, and 85.9 %T, with corresponding sheet resistances of 9.13×10^3, 5.99×10^3, and 3.38×10^3 Ω/sq. on glass. ITO-coated glass has sheet resistance of 25–30 Ω/sq. at normal temperature with light transparency >90 %. Due to the uniformity of ITO-coated glass, coalescent CuO@rGO (0.5, 0.1: 0.5, 0.5: 0.5, 0.1), exhibits transparencies of 89.7 %, 87.6 %, and 85.9 %, with sheet resistances of 15.69, 13.58 and 10.31 Ω/sq., respectively. The optical transparency of conductive surface facilitates efficient laser penetration and excitation of analytes during Raman measurements of SERS. The sheet resistance of coalescent 2D heterostructure CuO@rGO/ITO is lower than pristine ITO arises charge carrier path by the induction of CuO@rGO. rGO provides a high electrically conductive network due to sp^2 carbon, while CuO nanoparticles facilitate additional electron hoping side. When coalescent CuO@rGO structure deposited on ITO, form continuous bridge across ITO surface, that improve charge percolation and reduce scattering as like metallic Ag@rGO/ITO system [60].

Thoroughly investigating the electrical properties of the material, a cryostat instrument was used to perform Hall's effect measurements detailed explanation mentioned in (Supplementary SI). The meticulous value of all CuO, GO and coalescent CuO@rGO samples resistivity and carrier mobility summarized in (Table S1). The most effective composition, CuO@rGO (0.5, 1.0) has charge mobility (μ) 2.7×10^4 $cm^2/V\cdot s$ along with resistivity (ρ) 0.4×10^{-4} Ω·cm on ITO-coated glass (Fig. 5e, f) [61], then (μ) 4.8×10^3 $cm^2/V\cdot s$ and (ρ) 1.3×10^{-2} Ω·cm on glass (Fig. 5g, h) [62]. Current–voltage (I–V) measurements were conducted to better understand the electrical transport properties of the synthesized materials and assess the Ohmic behavior of undoped CuO, GO, and doped CuO@rGO thin films. Contact electrodes were fabricated using Ag on both ends of the film surface. The linear I—V characteristics of the films indicate an Ohmic contact between the prepared films and the Ag electrodes. On glass substrates, the current flow through GO is 0.005 mA

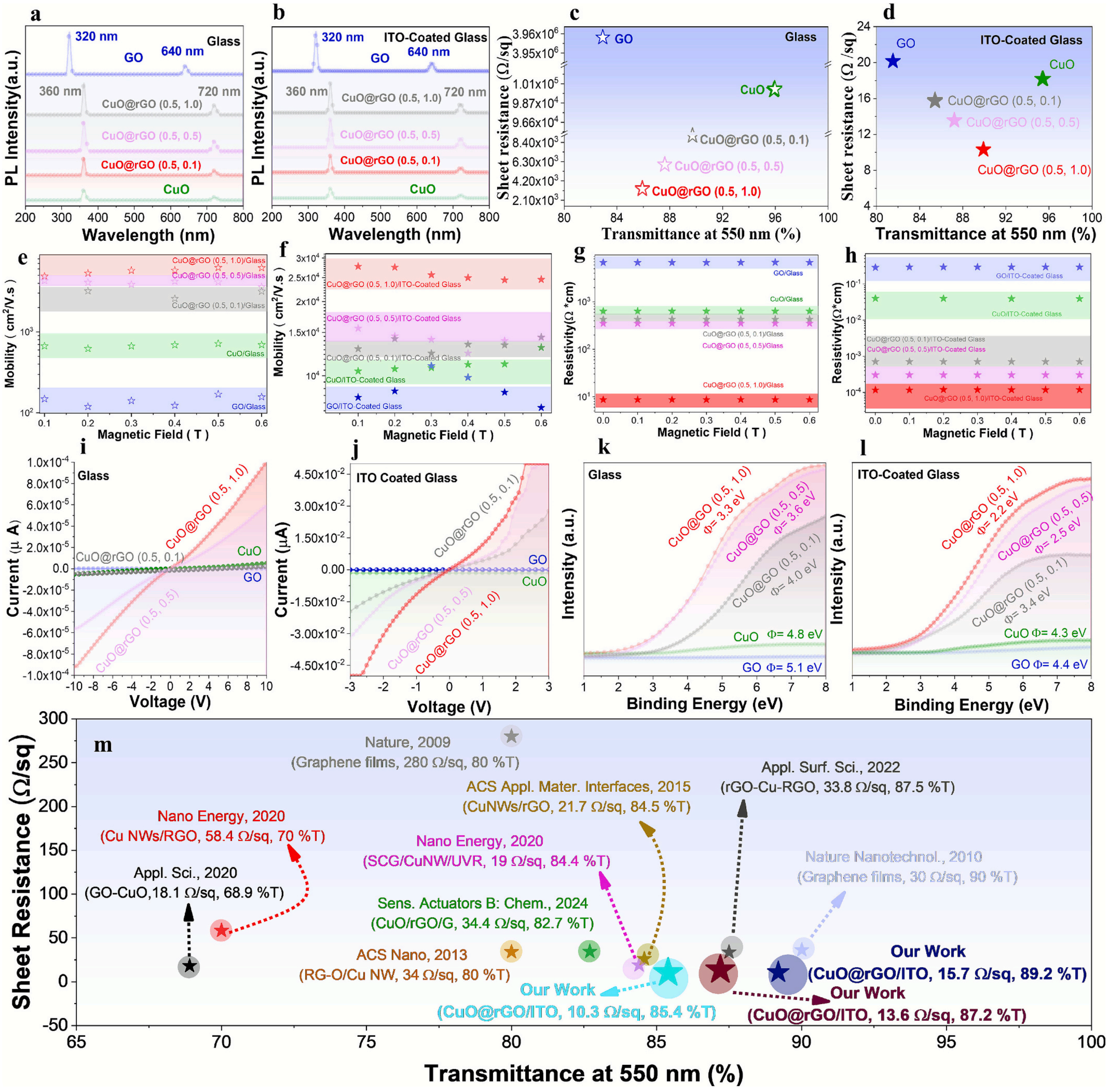

Fig. 5. Charge mobility beside work function variations with concentration. a, b) Photoluminescence spectra, c, d) Sheet resistances and light transmittances at 550 nm wavelength, e, f, g, h) Hall mobility and coefficient of Hall mobility resistance, i, j) I-V analysis. k, l) Ultraviolet photoelectron spectroscopy work function values of CuO, GO, CuO@rGO coating on glass and ITO-coated glass. m) Physical parameters of CuO, GO and coalescent CuO@rGO/ITO 2D heterostructures based our work in comparison with previous reports.

and through CuO is 0.07 mA under a bias voltage range (−10 V to10V). After the introduction of GO, the current increases from 2.0 mA to 19 mA at 3 V for CuO@rGO (0.5, 0.1), 2.0 mA to 32 mA at 3 V for CuO@rGO (0.5, 0.5), and it further increased to 46 mA for CuO@rGO (0.5,1.0) (Fig. 5i). When applied to ITO-coated glass, the current flow through GO is 0.8 mA and through CuO is 4 mA at a bias voltage (−3 V to 3 V). Current value gets increased from 1.8 mA to 27 mA at 3 V for CuO@rGO(0.5, 0.1), 1.0 mA to 46 mA at 3 V for CuO@rGO(0.5, 0.5), and it further increases up to 52 mA for CuO@rGO (0.5, 1.0) on glass (Fig. 5j). This improvement in current value is due to lower electrical resistivity with the addition of GO content into CuO [63].

The assessment of the work function determined by Ultraviolet photoelectron spectroscopy (UPS). Work function (Φ) represents the minimum energy required to extract an electron from the material's surface to vacuum. The work function of CuO, GO, and CuO@rGO samples was calculated from their UPS spectra by performing two linear extrapolations, one along the baseline and one at the secondary electron onset. Φ was thus calculated by subtracting the onset energy of secondary electron emission from the photon energy of helium (He) I radiation (21.2 eV), which provides information on surface electronic properties that are important for the interfacial charge transfer phenomenon. On glass substrate Φ was found for CuO (4.8 eV), GO (5.1 eV), CuO@rGO (0.5, 0.1) (4.0 eV), CuO@rGO (0.5, 0.5) (3.6 eV), CuO@rGO (0.5, 1.0) (3.3 eV) show in (Fig. 5k). In contrast ITO-coated glass: Φ of

CuO (4.3 eV), GO (4.4 eV), CuO@rGO (0.5, 0.1) (3.4 eV), CuO@rGO (0.5, 0.5) (2.5 eV), CuO@rGO (0.5, 1.0) (2.3 eV) depicted in (Fig. 5l). These values indicate inherent structural differences of electronic nature and surface potential, which are of utmost significance in controlling interfacial charge dynamics in heterostructures. Increasing rGO content adds more delocalization of electrons due to the larger π-conjugation in rGO, reducing the vacuum level and enabling ease of charge extraction. Thermal stability of CuO 97.72 %, GO 70.6 %, and CuO@rGO (0.5, 0.1), (0.5, 0.5), (0.5, 1.0), 95.55 %, 86.80 %, and 80.47 % compositions at 500 °C by TGA represented in (Supporting Information Fig. S11a–e). The

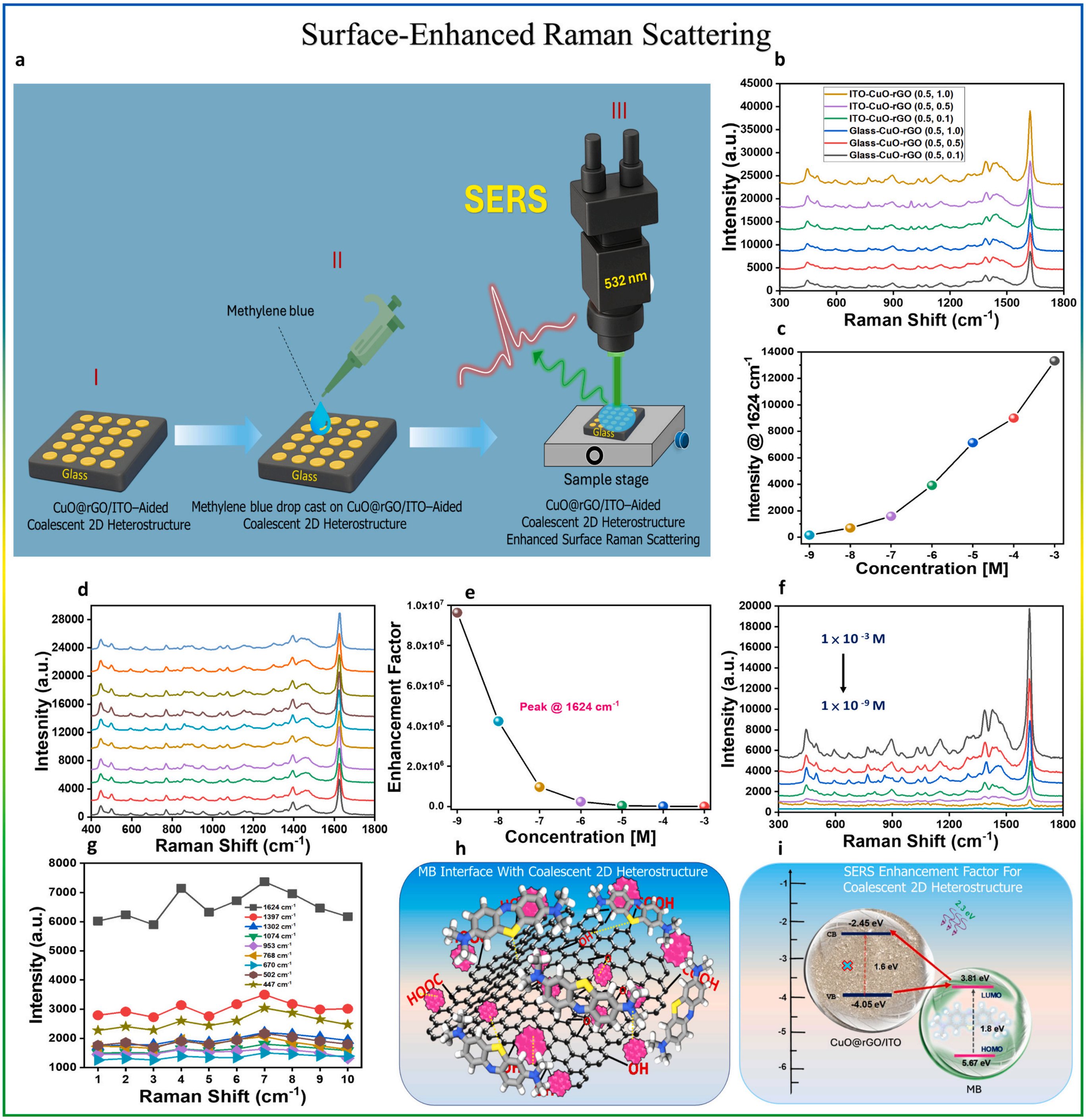

Fig. 6. SERS and ECS Analytical Interrogation. a) SERS characteristics of MB (0.0001) on coalescent CuO@rGO/ITO-coated glass 2D heterostructure and CuO@rGO/glass. b) SERS spectra of a series of MB concentration (10^{-3}–10^{-9} M) on coalescent 2D heterostructure (CuO@rGO (0.5,1.0)/ITO). c) Plot of [MB] (10^{-3}–10^{-9} M) on coalescent 2D heterostructure (CuO@rGO (0.5,1.0)/ITO) vs SERS intensity at 1624 cm^{-1}, d) AREFs as a function of [MB] (10^{-3}–10^{-9} M) on coalescent 2D heterostructure (CuO@rGO (0.5,1.0)/ITO). e, f) Batch-to-batch difference of [MB] 10^{-5} M on on coalescent 2D heterostructure (CuO@rGO (0.5,1.0)/ITO) and standard deviation of SERS peaks. g) MB molecules interaction with coalescent 2D heterostructure (CuO@rGO/ITO). h) Plausible SERS enhancement mechanism for MB on coalescent 2D heterostructure (CuO@rGO(0.5,1.0)/ITO). i) DPV responses at coalescent 2D heterostructure (CuO@rGO(0.5,1.0)/ITO) in 0.05 M PBS (pH 7.2) for additions of HQ concentrations (0.01–748.6 Mm). j) Linear calibration plot of HQ (Mm) vs. I_{pa} (μA). k) for ACP concentrations (0.01–909.0 μM). l) Corresponding linear calibration plot of ACP (Mm) vs. I_{pa} (μA) and m) simultaneous detection of HQ + ACP (2.1–308.7 μM). n) Linear calibration plots of HQ + ACP (Mm) vs. I_{pa} (μA). o) Electrochemical detection mechanism of HQ and ACP at coalescent 2D heterostructure CuO@rGO/ITO (0.5, 1.0)).

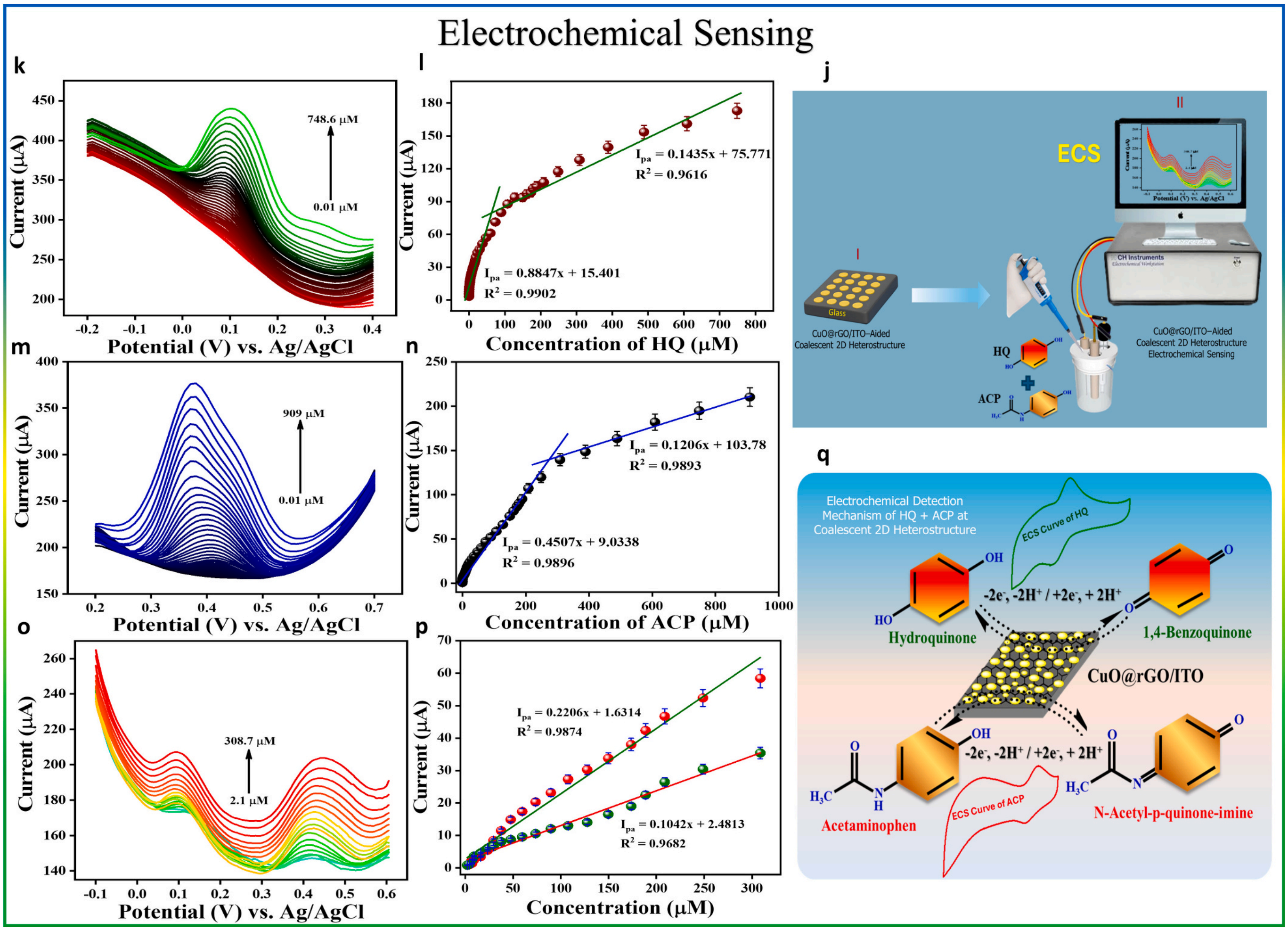

Fig. 6. (*continued*).

low work function facilitates photoinduced charge transfer between the substrate-analyte and high thermal stability prevents structural degradation of CuO@rGO heterostructures highly efficient for signal amplification and sensitivity [64]. For comparison with previous reports, (Fig. 5m) presents transparency of light and sheet resistance of our electrodes compared with other single 2D materials, metal oxides and coalescent CuO@rGO electrodes reported in literature (Table S2).

2.1. Advanced coalescent 2D heterostructure for SERS and ECS applications

Synthesized coalescent 2D heterostructures, consisting of rGO and CuO, were deposited on both conventional glass and ITO-coated glass substrates to investigate their SERS properties (Fig. 6a). Methylene blue (MB) was employed as Raman reporter to assess enhancement effects. Raman spectra of rGO, CuO, CuO@rGO, and MB (0.001 M) exhibited characteristic Raman peak assignments to (Supporting Information Fig. S12a, b). These spectral features confirm successful formation of individual materials and their heterostructures on both glass and ITO substrates. SERS spectra of CuO, rGO, and coalescent CuO@rGO in presence of the MB (0.001 M) demonstrated significant Raman signal enhancement, indicating the presence of SERS activity in both heterostructure and its individual components. Characteristic Raman peaks of MB provide crucial structural information (Supporting Information Fig. S12c). Specifically, C—N—C skeletal deformation is observed at 447 cm^{-1}, while C—S—C deformation appears at 502 cm^{-1}. Vibrational bands at 670, 768, and 953 cm^{-1} correspond to different C—H breathing modes. Additionally, peaks at 1302 cm^{-1} and 1396 cm^{-1} are identified to be in-plane ring deformation of C—H bonds and symmetrical stretching of C—N bonds, respectively. In-plane C—H bending mode is located at 768 cm^{-1}. Furthermore, NH_2 or C—C stretching, along with strong C—C ring stretching, is detected at 1624 cm^{-1} [65]. To evaluate their performance further, various compositions were investigated using a Raman spectrometer with MB at a concentration of 1×10^{-4} M. Notably, CuO@rGO heterostructures deposited on both glass and ITO-coated substrates exhibited high SERS activity as shown in (Fig. 6b). Raman spectra of MB adsorbed on heterostructures reveal that highest enhancement effect was observed for composition of coalescent 2D heterostructure CuO@rGO/ITO (0.5, 1.0). However, other compositions also demonstrated significant SERS activity, reinforcing potential of these nanostructured films for Raman signal enhancement. Consequently, coalescent 2D heterostructure CuO@rGO/ITO (0.5, 1.0) SERS substrate was further utilized for detection of MB at low concentrations, and its SERS performance was systematically evaluated. Fig. 6c demonstrates that fabricated SERS substrate enables a highly sensitive detection of methylene blue (MB) at a concentration of 1×10^{-9} M (nanomolar, nM). As depicted in (Fig. 6d), a reduction in MB concentration correlates with a decline in signal intensity, thereby highlighting concentration-dependent influence on peak intensity. Analytical Raman enhancement factor (AREF) for SERS studies was determined following established methodologies, with a comprehensive discussion provided in (Supporting Information Fig. S12d). AREF values, plotted as a function of concentration (molarity) vs calculated AREF values for characteristic Raman peak at 1624 cm^{-1} as shown in (Fig. 6e). Notably, observed trend indicates that a decrease in MB concentration results in an increase in AREF, underscoring superior performance of SERS substrate equal to 9.62×10^6 for 1×10^{-9} M.

Furthermore, batch-to-batch reproducibility of SERS substrate, fabricated under identical conditions, exhibited a consistent SERS enhancement profile (Fig. 6f). A total of ten SERS substrates were synthesized and employed for spectral measurements using MB at a concentration of 10^{-5} M. Calculated relative standard deviation (RSD) values ranged between 5 % and 10 % (Fig. 6g), confirming the high reproducibility of coalescent 2D heterostructure CuO@rGO/ITO (0.5, 1.0) SERS substrate. Additionally, SERS spectra were recorded at ten distinct locations on a single substrate across varying concentrations, with corresponding results and detailed discussion provided (Supporting Information Fig. S13a–n). We systematically analyzed the underlying enhancement mechanism responsible for superior SERS performance, which is aided by band gap alignment [66], charge transfer efficiency, and molecular adsorption via π–π interactions. Additionally, (Fig. 6h, i) the role of homogeneous coating technique (spin coating) in facilitating uniform substrate coverage was evaluated, with an in-depth discussion presented in (Supplementary). Performance of the developed SERS substrate was systematically compared with previously reported SERS substrates aided with key parameters, including preparation and fabrication methods, analyte type, laser source, enhancement factor (EF), spectral repeatability (relative standard deviation, RSD), limit of detection, and underlying SERS mechanism (Table 1). Comparative analysis highlights that coalescent 2D heterostructures (CuO@GO/ITO) (0.5, 1.0) exhibit exceptional SERS enhancement and superior performance, surpassing many previously reported SERS platforms. This superior overall performance makes it a strong candidate for future SERS assays in ultra-sensitive detection.

Electrochemical preparation and instrumentation setup clearly are given in (Fig. 6j). Performance of the prepared electrodes CuO@rGO/ITO with varied in volume ratios (0.5, 0.1) (0.5,0.5) (0.5, 1.0) as well as that of pristine ITO, CuO/ITO and rGO/ITO are investigated using Cyclic Voltammetry (CV) (Supporting Information Fig. S10) and Differential Pulse Voltammetry (DPV) techniques. Hydroquinone (HQ) and Acetaminophen (ACP) were important analytes for both individual and simultaneous electrochemical detection widely studied in electrochemical sensing due to their exceptional biomedical, environmental significance and well-documented redox chemistry. These molecules serve as model analytes to evaluate the sensitivity, selectivity, and linear dynamic range of electrochemical sensors. In contrast to conventional electrode materials, such as bare glassy carbon or metallic electrodes, HQ and ACP exhibit improved linearity and more favorable electrocatalytic responses when detected with sensors that incorporate coalescent 2D heterostructures materials. These performance improvements are derived from the synergistic effects at the heterointerface, which facilitate rapid charge transfer and increase the active surface area, leading to enhanced analytical performance in the form of expanded linear ranges, reduced detection limits, and improved reproducibility. The analysis was conducted using a three-electrode system, which included various modified electrodes as the working electrode, a saturated Ag/AgCl electrode as the reference, and a platinum (Pt) wire as the counter electrode. For the initial electrochemical analysis, a 0.05 M phosphate buffer solution (PBS) at pH 7.2 was used as the electrolyte, containing 200 μM HQ and ACP, with a scan rate of 50 mV/s (Supporting Information Fig. S14a, b). From these, CuO@rGO/ITO (0.5, 1.0) electrode indicate that both individual and simultaneous analyses yielded higher redox peak currents at lower redox potentials for HQ $I_{pa}/I_{pc} = 264.32\ \mu A/-207.27\ \mu A$ at $E_{pa}/E_{pc} = 0.147\ V/-0.006\ V$ and for ACP $I_{pa}/I_{pc} = 297.28\ \mu A/-124.96\ \mu A$ at $E_{pa}/E_{pc} = 0.443\ V/0.337\ V$ compared to all other modified electrodes. These findings indicate an enhanced electron transport rate, catalytic activity, and electrical conductivity of the sensor probe. Additionally, important parameters such as the effects of concentration and scan rate on the individual detection of HQ and ACP, as well as their simultaneous detection, were investigated by varying one parameter while keeping the other constant.

Based on the obtained CV data, the proposed electrochemical detection mechanisms for HQ and ACP are proposed (Fig. 6q). In the electrochemical reaction at the surface of CuO@rGO/ITO (0.5, 1.0) electrode, HQ loses two protons (H^+) and two electrons (e^-) and is oxidized to form 1,4-benzoquinone. This process is reversible, as 1,4-benzoquinone can gain $2H^+$ and $2e^-$ to be reduced back to its original state, HQ [86]. In a similar way, ACP losses $2H^+$, $2e^-$ and oxidized to form *N*-acetyl-p-benzoquinone-imine and then at negative potential oxidized product reduced to ACP vice-versa [87]. ACP has undergone

Table 1
SERS performance of coalescent 2D heterostructure (CuO@rGO/ITO) comparison with the previously reported works.

SERS substrates	Fabrication method	Analyte/laser	Enhancement factor/relative standard deviation	LOD [M]	Refs.
CuONWs@TiO_2	Atomic layer Deposition+ Immerse/3 h	R6G/532 nm	NA/6.61 %@611 cm^{-1}	10^{-7}	[19]
CuO ultra-fine particles/TiO_2	Sol-hydrothermal method	4-mercaptobenzoic acid (4-MBA)/ 532 nm	8.87×10^6/NA	10^{-10}	[67]
Ag/CuO NWs/Cu_2O composite	Nanosecond Laser Ablation + Thermal Oxidation + Ag deposition	MG/visible light	NA/ N/A	10^{-5}	[68]
PAN/N-GQDs	Dip coating technique	MB / 532 nm	1×10^4 /NA	NA	[69]
2 M-WS_2 nanosheets	Chemical exfoliation	MB/532 nm	NA / 10.5 %	10^{-8}	[70]
$CH_3NH_3PbBr_3$@Al_2O_3	In situ growth $MAPbBr_3$ with Al_2O_3 by magnetron sputtering.	MB/633 nm	2.45×10^5/NA	10^{-9}	[71]
Ultrathin film CuS	Chemical synthesis+ Self-assembly	R6G / 785 nm	7.2×10^4 / N/A	10^{-9}	[72]
RGO-wrapped Au NPs	chemical reduction method	R6G / 532 nm	1.01×10^{11} / N/A	NA	[73]
Cu_2O nanospheres	Chemical reduction+ Self-assembly	R6G / 785 nm	N/A / N/A	10^{-12}	[74]
ZnTPP/Ag(111)	Thermal evaporation onto Ag(111)	ZnTPP / 532 nm	N/A / N/A	NA	[75]
Ti_3C_2–OH/F sheets	Delamination in HF by DMSO intercalation	MB/632.8 nm	N/A / N/A	10^{-8}	[76]
MoS2–graphene	Chemical exfoliation	R6G / 532 nm	N/A / N/A	NA	[77]
Plasma-enhanced GQDs	Chemical Vapor Deposition	R6G / 532 nm	2.35×10^3/NA	10^{-9}	[78]
MoS_2/Ag/rGO composite	Hydrothermal Method	MB / 632.8 nm	NA/10 %	10^{-7}	[79]
Au/Fe_3O_4/MIL-101(Cr) (AF-MIL)	Hydrothermal Method	R6G / 632.8 nm	NA/4.48 %	10^{-8}	[80]
Etched Au@SiO_2 NRs	Solvent Evaporation Assembly	Crystal Violet / 633 nm	1.28×10^5/NA	NA	[81]
TiO_2-a1 Aerogels	Sol–gel method	MBA / 532 nm	NA/NA	10^{-7}	[82]
MoO_2 Nanodumbbells	Hydrothermal synthesis	R6G / 532 nm	3.75×10^6/5 %	10^{-7}	[83]
DFH-4 T	Modified PVD	MB / 785 nm	3.4×10^3/NA	10^{-5}	[84]
Cu-deposited np-Ag	Electrochemical reduction	CO_2 / 532 nm	6.35×10^5/NA	NA	[85]
CuO@rGO/ITO	Solvothermal+ Spin coating	MB/532 nm	9.62×10^6/5–10 %	10^{-9}	This work

quasi-reversible redox process. From this analysis an equal number of protons and electrons are involved in electrochemical reaction of both HQ and ACP, and it can be experimentally proven that simultaneous detection is possible. We observe that CuO@rGO/ITO (0.5, 1.0) heterostructures are observed as highly efficient electron donors/acceptors with negligible electron-transport confrontation, synergistic recombination and strong $\pi - \pi$ and electrostatic interactions between analytes and our electrode. The effect of concentrations and scan rates analysis toward the analysis of HQ and ACP at CuO@rGO/ITO (0.5, 1.0) with their detailed explanation are provided in (Supporting Information Fig. S14c–n), CuO@rGO/ITO (0.5, 1.0) electrode was used for quantitative analysis of HQ and ACP, assessing its limit of detection, linear range and selectivity through DPV in 0.05 M PBS pH of 7.2. Distinct oxidation currents for HQ and ACP at specific potentials (−0.2 to 0.4 and −0.2 to 07), confirm that the coalescent 2D heterostructure CuO@rGO/ITO (0.5, 1.0) electrode is suitable for simultaneous, selective sensing. DPV curves for concentration ranges of 0.01–748.6 Mm for HQ (Fig. 6k) and 0.01–909.0 Mm for ACP (Fig. 6m), as well as for a combination of HQ + ACP with 2.1–308.7 Mm (Fig. 6o), showing a slight shift in peak currents due to additional molecular layers. Calibration plots and regression analysis are presented in (Fig. 6l, n, p), revealing linear fits of HQ and ACP for individual and two linear fits for simultaneous detection respectively. At lower concentrations, a rapid molecular movement leads to a quicker response while at higher concentrations it can be significantly hindered that results in slower responses. The limit of detection (LOD) was determined using the following equation

$$\mathrm{LOD} = 3\mathrm{S}/\mathrm{N}$$

where S signifies standard deviation from blank measurements, and N is the slope of the linear plot between concentration vs anodic peak currents which yields 4.7 nM for HQ, 6.3 nM for ACP respectively. Additionally, the sensitivity of the proposed sensor calculated using the following formula

$$\mathrm{Sensitivity} = \mathrm{Slope}/\mathrm{electrochemical\ active\ surface\ area}$$

From this equation the sensitivity was found to be 1.7740 μA μM^{-1} cm^{-2} for HQ and 0.9037 μA μM^{-1} cm^{-2} for ACP sensor. A comparison of the sensing capabilities of our sensor with previous reports is summarized in (Table 2), indicating that the coalescent 2D heterostructure CuO@rGO/ITO (0.5, 1.0) electrode provides superior electrochemical detection, yielding low LOD and demonstrating wide linearity. This enhanced performance is attributed to high electrical conductivity, enhanced specific surface area, numerous active sites and synergistic effects of CuO and rGO on ITO on glass surface, along with the innovative spin-coating methodology employed. Selectivity of the proposed sensor was assessed by DPV to attain its practical applicability of proposed sensor. We used many similar structural compounds for the selectivity analysis and results showed that the sensor had a consistent and patternable response to the target analyte, and there was insignificant interference by these interfering species as illustrated in (Supporting Information Fig. S15a, b). In addition to that, the practical applicability of the proposed sensor was evaluated using tap water sample for both HQ and ACP which results adequate recoveries with low levels of RSD and the obtained DPV curves displayed in (Supporting Information Fig. S15c, d). The overall recovery results were calibrated through standard addition method and are tabulated in Table S3 using the following equation.

$$\mathrm{Recovery}\ (\%) = (\mu\mathrm{M\ analyte\ found}/\mu\mathrm{M\ analyte\ expected}) \times 100$$

Furthermore, the individual sensing capability of co-existing HQ and ACP is also investigated and corresponding DPV responses displayed in (Supporting Information Fig. S16a, b) which demonstrate DVP responses in excellent linearity (Supporting Information Fig. S16c, d). Measurement reproducibility was confirmed by a low relative standard deviation (RSD) of 1.93 % in DPV using five independently fabricated electrodes (Supporting Information Fig. S16e). Stability testing of electrode over 20 days that stored at room temperature, with measurements every five days (Supporting Information Fig. S16f), revealed that oxidation peak current retained 96.4 % of its initial value, with an RSD of 2.20 %, indicating excellent stability of proposed CuO@rGO/ITO (0.5, 1.0) sensor.

Our work creates framework for CuO@rGO/ITO 2D heterostructure stability and multifunctional functionality, certain limitations to be mentioned are that hydrothermal synthesis as supplemented with spin-coating, as efficient in laboratory scale, introduce batch-to-batch variability of film thickness and interface binding, which cause of concern for reproducibility on a large industrial process scale. Simulation results facilitate critical insights about interfacial bonding and adsorption energy. However, these models are made using idealized supercells and short simulation times that do not fully match defect dynamics, long-term disorder, or large-area heterogeneity inherent in actual devices. Moreover, electrochemical treatment was carried out with model analytes in highly controlled laboratory settings, and their extension to more complex systems related to biological fluids or industrial effluents

Table 2

Comparative analysis of electrochemical detection of HQ and ACP.

Analyte	Modified electrode	Technique	Linear range (μM)	LOD (μM)	Sensitivity (μA μM^{-1} cm^{-2})	Refs.
Hydroquinone (HQ)	CaM@rGO/GCE	DPV	0.05–105	0.0086	0.2858	[88]
	PANi-Fe_2O_3_rGO/GCE	DPV	0.1–550	0.006	NA	[89]
	Cu SAs/N-CSs/CP	DPV	1–324	0.33	0.2349	[90]
	PtNPs@CPOFs MWCNTs/GCE	DPV	6–500	0.66	NA	[91]
	UiO-67-CPE	DPV	5–300	0.0036	NA	[92]
	Cu(II)/AgNP/GCE	DPV	2.81–8.3	0.00082	NA	[93]
	Ag/g-C_3N_4/GCE	DPV	0.9–999	5.9	0.06	[94]
	AuNPs/C	AMP	0.01–400	0.00235	0.34	[95]
	PEDOT:PSS	DVP	0.1–10	0.05	0.9	[96]
	Graphene QDs	AMP	0.1–50	0.01	1.5	[97]
	CuO@rGO/ITO (0.5, 1.0)	DPV	0.01–748.6	0.0047	1.7740	This work
Acetaminophen (ACP)	$SrWO_4$/GCE	DPV	0.01–25.90	0.008	NA	[98]
	MWCNT-βCD (SE)/GCE	LSV	0.01–15	0.0025	NA	[99]
	FeCo@C/GCE	DPV	0.001–0.8	0.59	NA	[100]
	Cd-MOF@MoS_2/GCE	DPV	0.020–200	0.0098	0.6012	[101]
	UN@Ti_3C_2-C/GCE	DPV	0.032–160	0.010	1.235	[102]
	CNTs/ITO	DPV	0.1–300	0.04	N/A	[103]
	AuNM/PE/PLLA–PTMC	LSV	0.01–100	0.00397	0.00529	[104]
	Bi_2O_3 Nanorod/SPE	DPV	10–210	0.037	0.02	[105]
	AuNPs/Nb_4C_3-MXene	SWV	0.0001–0.1	0.0001462	N/A	[106]
	Fe/Cu@C	DPV	0.01–7	0.025	N/A	[107]
	CuO@rGO/ITO (0.5, 1.0)	DPV	0.01–909.0	0.0063	0.9037	This work

remains to be manifested. Although heterostructures were observed to be capable of retaining stable Raman enhancement and electrochemical sensitivity for ambient exposure, comprehensive durability testing under more strenuous conditions achieve confidence in long-term operational reliability. Cumulatively taken, these factors do not devalue the potency of existing results but rather indicate seminal avenues for future research that have the potential to bridge the evidence gap between proof-of-concept demonstrations toward robust, scalable device integration.

In the wake of the findings of this study, there are various avenues of furthering CuO@rGO/ITO 2D heterostructures. From processing perspective, work on developing optimized methods of deposition to achieve wafer-scale uniformity and integrating roll-to-roll or printing techniques could accelerate their transfer into industrially relevant platforms. At device level, exploration of additional conductive oxides or hybrid electrodes can potentially unlock even greater stability to mechanical stress, while compositional tuning of the CuO@rGO ratio can optimize sensitivity to specific analytes. Beyond model redox systems studied, platform validation in demanding environments such as biological fluids, industrial effluent, or gas-phase analytes will be necessary to demonstrate broad utility. At a theoretical level, multiscale simulations that incorporate defect motion, disorder evolution, and long-term environmental stressors could provide more mechanistic information about durability and guide rational design of revolutionary heterostructures. Complementing each other, these approaches are viable paths to further develop the proof-of-concept developed here into scalable, multifunctional sensing technologies for real-world applications.

3. Conclusion

Advanced SERS and ECS applications were successfully integrated with coalescent 2D heterostructures (CuO@GO/ITO) via hydrothermal method, providing a multifunctional platform with significant advantages over traditional materials applied in SERS and ECS applications. Advanced coalescent 2D heterostructures (CuO@GO/ITO) exhibit excellent electrocatalytic activity, sensitivity, and selectivity, with surface roughness 17.1 nm, sheet resistance 10.3 Ω/sq., transparency of 85.4 %, charge mobility 2.7×10^4 cm^2/V·s, current flow 52 mA and work function 2.2 eV. Theoretical investigation via DFT and AIMD simulations further confirmed water adsorption ($E_{ads} = -0.73$ to -0.13 eV), robust strong coalescent 2D heterostructure CuO@GO/ITO binding energy (E_b-5.54 eV), and suitable charge transfer for SERC and ECS performance. This interface enables SERS enhancement factor 9.62×10^6, by facilitating methylene blue efficacy 1×10^{-9} M. ECS revealed higher linearity with a detection of limit and sensitivity 4.7 nM (1.7740 μA μM^{-1} cm^{-2}) for HQ, 6.3 nM (0.9037 μA μM^{-1} cm^{-2}) for ACP and its practical applicability were confirmed through tap water sample analysis that results outstanding recoveries. The ability of CuO@rGO/ITO to carry current and transmit light efficiently allows the platform to be used for integrated SERS and electrochemical sensing in transparent displays. Our coalescent 2D heterostructure CuO@rGO/ITO constitute enhanced electrocatalytic activity, reversible signal response, and superior interfacial charge transfer. Thereby, these exceptional results together with their scalable fabrication and environmental stability provide them with potential to become a promising platform for next generation multifunctional, diminutive sensors, electronics, and optoelectronics.

4. Methods

4.1. Fabrication of coalescent 2D advanced heterostructure (CuO@rGO/ITO) via solvothermal method

Hummer's method is used on an industrial level to produce large amounts of graphite oxide yield. This method is not costly, and we use this method in our present work. Synthesis process of GO involved 5 g of stirring of graphite powder, 115 ml of H_2SO_4, and 2.5 g of $NaNO_3$ for 40 min. Subsequently, 15 g of potassium permanganate was slowly added at low temperature, followed by heating at room temperature for 3 h. Afterward, 700 ml of water was added, and addition of H_2O_2 terminated the reaction. The resulting mixture was washed with HCl and water, then centrifuged and dried to obtain solid form of GO (Supporting Information Fig. S2, steps 1–4). To prepare the solution, 55 mg of CuO were added to 100 ml of DI water. Mixture was sonicated for 30 mins and then stirred for 6 h on a hotplate. Subsequently, mixture was centrifuged at 2000 rpm for 5 mins to obtain a concentration of CuO in DI water of 0.5 mg/ml. Various concentrations of GO and CuO solutions were utilized to create a mixture resulting in coalescent CuO@rGO, where CuO is attached to surface of rGO nanoflakes sheets (Supporting Information Fig. S2, steps 5–6).

4.2. Computational method

DFT calculations were performed using the Quantum Espresso (QE) software package [33]. Ion-electron interactions were described by projector-augmented wave (PAW) pseudopotential method [108]. To account for electron exchange-correlation effects, generalized gradient approximation (GGA) parameterized by Perdew-Burke-Ernerhof (PBE) was employed [109]. Van der Waals interactions were corrected using semiempirical DFT-D3 method within Grimme scheme [110]. A kinetic energy cutoff of 50 Ry was chosen for plane-wave function expansion and 500 Ry for charge density and potential. Gaussian smearing method with a Monkhorst-Pack k-mesh of 3 × 3 × 1 was utilized for Brillouin-zone integration. Convergence criteria for energy and force were set at 10^{-6} eV and 0.01 eV/Å, respectively. Further detailed information on computational methods is described in (Supplementary).

4.3. SERS and ECS applications

Coalescent CuO@rGO prepared by spin on glass and ITO-coated glass substrates. Synthesis is characterized by surface-enhanced Raman scattering (SERS) and electrochemical technique analyses, which include cyclic voltammetry (CV) and differential pulse voltammetry (DPV). For SERS, methylene blue (MB) served as Raman reporter for enhancement evaluation and the substrates were dried following deposition of the molecular beam (MB) coating for 10 min at 70 °C using a hot air oven. SERS was measured using a 532 nm laser (10 s, 1 accumulation), while electrochemical detection using phosphate buffer solution (PBS) at pH 7.2 was adopted for hydroquinone (HQ) and acetaminophen (ACP). Coalescent CuO@rGO provide high electron conductivity, strong molecular adsorption, and excellent catalytic activity illusion due to which excellent SERS and electrochemical behavior were achieved.

CRediT authorship contribution statement

Muhammad H. Nawaz: Software, Investigation, Formal analysis, Data curation, Writing – review & editing, Writing – original draft. **S. Santhoshkumar:** Data curation, Writing – review & editing. **Thi H. Ho:** Data curation, Writing – review & editing. **Balamurugan Arumugam:** Data curation, Writing – review & editing. **Mohamed Gamal Mohamed:** Data curation. **Tuan V. Vu:** Data curation. **Yousra.M. Nabil:** Data curation. **Mohammed G. Kotp:** Data curation. **Li-Wei Tu:** Data curation. **Hung-Duen Yang:** Data curation. **Ahmed F.M. EL-Mahdy:** Data curation. **Shiu-Ming Huang:** Data curation. **Po-Ling Chang:** Data curation. **Trung Nguyen-Thoi:** Data curation. **Shiao-Wei Kuo:** Data curation. **Wei-Lung Tseng:** Data curation. **Kin-Man Yu:** Writing – review & editing. **Feng-Chuan Chuang:** Supervision, Project administration, Funding acquisition, Writing – review & editing. **Phuong V. Pham:** Supervision, Methodology, Investigation, Funding acquisition, Data curation, Conceptualization, Writing – review & editing, Writing – original draft.

Declaration of competing interest

The authors declare no competing interests.

Acknowledgments

The authors thank Prof Ting-Chang Chang (IEEE Fellow) for the assistance in I-V curve measurement. This work is supported by the National Science and Technology Council, Taiwan (Grant No.: NSTC-114-2112-M-110-015, NSTC-112-2112-M-110-004-MY3 and NSTC-110-2112-M-110-013-MY3).

Appendix A. Supplementary data

Supplementary data to this article can be found online at https://doi.org/10.1016/j.cej.2025.171521.

Data availability

The data that support the findings of this study are available from the corresponding author upon reasonable request.

References

[1] H.W. Chen, J.H. Lee, B.Y. Lin, S. Chen, S.T. Wu, Liquid crystal display and organic light-emitting diode display: present status and future perspectives, Light Sci. Appl. 7 (2017) 17168–17168, https://doi.org/10.1038/LSA.2017.168; TECHMETA.

[2] A.C. Ferrari, F. Bonaccorso, V. Fal'ko, K.S. Novoselov, S. Roche, P. Bøggild, S. Borini, F.H.L. Koppens, V. Palermo, N. Pugno, J.A. Garrido, R. Sordan, A. Bianco, L. Ballerini, M. Prato, E. Lidorikis, J. Kivioja, C. Marinelli, T. Ryhänen, A. Morpurgo, J.N. Coleman, V. Nicolosi, L. Colombo, A. Fert, M. Garcia-Hernandez, A. Bachtold, G.F. Schneider, F. Guinea, C. Dekker, M. Barbone, Z. Sun, C. Galiotis, A.N. Grigorenko, G. Konstantatos, A. Kis, M. Katsnelson, L. Vandersypen, A. Loiseau, V. Morandi, D. Neumaier, E. Treossi, V. Pellegrini, M. Polini, A. Tredicucci, G.M. Williams, B. Hee Hong, J.H. Ahn, J. Min Kim, H. Zirath, B.J. Van Wees, H. Van Der Zant, L. Occhipinti, A. Di Matteo, I. A. Kinloch, T. Seyller, E. Quesnel, X. Feng, K. Teo, N. Rupesinghe, P. Hakonen, S. R.T. Neil, Q. Tannock, T. Löfwander, J. Kinaret, Science and technology roadmap for graphene, related two-dimensional crystals, and hybrid systems, Nanoscale 7 (2015) 4598–4810, https://doi.org/10.1039/C4NR01600A.

[3] P.V. Pham, S.C. Bodepudi, K. Shehzad, Y. Liu, Y. Xu, B. Yu, X. Duan, 2D Heterostructures for ubiquitous electronics and optoelectronics: principles, opportunities, and challenges, Chem. Rev. 122 (2022) 6514–6613, https://doi.org/10.1021/ACS.CHEMREV.1C00735.

[4] P.V. Pham, T.H. Mai, H.B. Do, M. Vasundhara, V.H. Nguyen, T. Nguyen, H. Van Bui, V.D. Dao, R.K. Gupta, V.K. Ponnusamy, J.H. Park, Layer-by-layer thinning of two-dimensional materials, Chem. Soc. Rev. 53 (2024) 5190–5226, https://doi.org/10.1039/D3CS00817G.

[5] C. Gu, A.B. Jia, Y.M. Zhang, S.X.A. Zhang, Emerging electrochromic materials and devices for future displays, Chem. Rev. 122 (2022) 14679–14721, https://pubs.acs.org/doi/full/10.1021/acs.chemrev.1c01055 (accessed March 24, 2025), https://doi.org/10.1021/ACS.CHEMREV.1C01055.

[6] L. Zeng, Z. Cheng, J.A. Fan, L.S. Fan, J. Gong, Metal oxide redox chemistry for chemical looping processes, Nat. Rev. Chem. 2 (2018) (2018) 349–364, https://doi.org/10.1038/S41570-018-0046-2;SUBJMETA.

[7] X. Ma, T. Yang, D. He, X. Gao, W. Jiang, D. Li, Y. Sun, X. Lin, J. Xu, H. Wang, X. Tai, Y. Lin, T. Yao, H. Zhou, Y. Wu, Carbonate shell regulates CuO surface reconstruction for enhanced CO2 electroreduction, Nat. Synth. 4 (2024) 53–66, doi:038/S44160-024-00672-9;SUBJMETA.

[8] L. Xie, P. Wang, Y. Li, D. Zhang, D. Shang, W. Zheng, Y. Xia, S. Zhan, W. Hu, Pauling-type adsorption of O2 induced electrocatalytic singlet oxygen production on N–CuO for organic pollutants degradation, Nat. Commun. 13 (2022) 1–11, https://doi.org/10.1038/S41467-022-33149-4;TECHMETA.

[9] Z. Wang, N. Qureshi, S. Yasin, A. Mukhin, E. Ressouche, S. Zherlitsyn, Y. Skourski, J. Geshev, V. Ivanov, M. Gospodinov, V. Skumryev, Magnetoelectric effect and phase transitions in CuO in external magnetic fields, Nat. Commun. 7 (2016) 1–8, https://doi.org/10.1038/NCOMMS10295;TECHMETA.

[10] V.P. Pham, K.H. Kim, M.H. Jeon, S.H. Lee, K.N. Kim, G.Y. Yeom, Low damage pre-doping on CVD graphene/Cu using a chlorine inductively coupled plasma, Carbon N. Y. 95 (2015) 664–671, https://doi.org/10.1016/J.CARBON.2015.08.070.

[11] M.H. Nawaz, M.K. Shahid, R.K. Gupta, R. Jalil, F.C. Chuang, P.V. Pham, Flatland of graphene's derivatives: classification, synthesis, mechanisms, role of defects, applications, and prospectives, Coord. Chem. Rev. 528 (2025) 216421, https://doi.org/10.1016/J.CCR.2024.21642.

[12] K.M. Chahrour, P.C. Ooi, A.A. Nazeer, L.A. Al-Hajji, P.R. Jubu, C.F. Dee, M. Ahmadipour, A.A. Hamzah, CuO/Cu/rGO nanocomposite anodic titania nanotubes for boosted non-enzymatic glucose biosensors, New J. Chem. 47 (2023) 7890–7902, https://doi.org/10.1039/D3NJ00666B.

[13] Y. Chen, Z. Wang, G. Jin, S. Zhu, W. Liu, Achieving high strengthening efficiency and good balance between strength and ductility/electrical conductivity in the laminated RGO/copper composites, ACS Appl. Electron. Mater. 6 (2024) 5903–5913, https://doi.org/10.1021/ACSAELM.4C00882.

[14] Y. Guo, H. Wang, X. Ma, J. Jin, W. Ji, X. Wang, W. Song, B. Zhao, C. He, Fabrication of ag-Cu2O/reduced graphene oxide nanocomposites as surface-enhanced Raman scattering substrates for in situ monitoring of peroxidase-like catalytic reaction and biosensing, ACS Appl. Mater. Interfaces 9 (2017) 19074–19081, https://doi.org/10.1021/ACSAMI.7B02149.

[15] T. Haldar, J.W. Shiu, R.X. Yang, W.Q. Wang, H.T. Wu, H.I. Mao, C.W. Chen, C. H. Yu, Exploring MOF-derived CuO/rGO heterostructures for highly efficient room temperature CO2 sensors, ACS Sens. 9 (2024) 5856–5865, https://doi.org/10.1021/ACSSENSORS.4C01397/ASSET/IMAGES/LARGE/SE4C01397_0005.JPEG.

[16] F. Zhou, J. Wang, Y. Tang, S. Liu, Y. Du, W. Jing, Y. Li, L. Hai, W. Li, F. Gao, Investigation on the surface morphologies of reduced graphene oxide coating on the interfacial characteristics and electro-catalytic capacity of enzymatic glucose sensors, Nanotechnology 34 (2022) 015501, https://doi.org/10.1088/1361-6528/AC96FB.

[17] X. Tang, Q. Hao, X. Hou, L. Lan, M. Li, L. Yao, X. Zhao, Z. Ni, X. Fan, T. Qiu, Exploring and engineering 2D transition metal dichalcogenides toward ultimate SERS performance, Adv. Mater. 36 (2024) 2312348, https://doi.org/10.1002/ADMA.202312348.

[18] I. Shlesinger, J. Vandersmissen, E. Oksenberg, E. Verhagen, A.F. Koenderink, Hybrid cavity-antenna architecture for strong and tunable sideband-selective molecular Raman scattering enhancement, Sci. Adv. 9 (2023) eadj4637, https://doi.org/10.1126/SCIADV.ADJ4637.

[19] W. Yin, S. An, T. Cheng, L. Jiang, Y. Cao, Enhancing SERS sensitivity of semiconductors through constructing CuO@TiO2 heterojunctions via atomic layer deposition, Appl. Surf. Sci. 672 (2024) 160820, https://doi.org/10.1016/j.apsusc.2024.160820.

[20] L. Andronic, C. Abreu-Jaureguí, J. Silvestre-Albero, Construction of TiO2@Cu2O-CuS heterostructures integrating RGO for enhanced full-spectrum photocatalytic degradation of organic pollutants, J. Alloys Compd. 994 (2024) 174682, https://doi.org/10.1016/j.jallcom.2024.174682.

[21] H. Ma, S.Q. Pan, W.L. Wang, X. Yue, X.H. Xi, S. Yan, D.Y. Wu, X. Wang, G. Liu, B. Ren, Surface-enhanced Raman spectroscopy: current understanding, challenges, and opportunities, ACS Nano 18 (2024) 14000–14019, https://doi.org/10.1021/ACSNANO.4C02670.

[22] S. Santhoshkumar, W.S. Wei, M. Madhu, W. Bin Tseng, W.L. Tseng, Chemically engineered sulfur vacancies on few-layered molybdenum disulfide nanosheets for remarkable surface-enhanced Raman scattering activity, J. Phys. Chem. C. 127 (2023) 8803–8813, https://doi.org/10.1021/ACS.JPCC.3C01044.

[23] S.M. Sibug-Torres, D.B. Grys, G. Kang, M. Niihori, E. Wyatt, N. Spiesshofer, A. Ruane, B. de Nijs, J.J. Baumberg, In situ electrochemical regeneration of nanogap hotspots for continuously reusable ultrathin SERS sensors, Nat. Commun. 15 (2024) 1–13, https://doi.org/10.1038/S41467-024-46097-Y; TECHMETA.

[24] X. Zhao, X. Liu, D. Chen, G. Shi, G. Li, X. Tang, X. Zhu, M. Li, L. Yao, Y. Wei, W. Song, Z. Sun, X. Fan, Z. Zhou, T. Qiu, Q. Hao, Plasmonic trimers designed as SERS-active chemical traps for subtyping of lung tumors, Nat. Commun. 15 (2024) 1–11, https://doi.org/10.1038/S41467-024-50321-0;TECHMETA.

[25] Y. Zhao, A. Kumar, Y. Yang, Unveiling practical considerations for reliable and standardized SERS measurements: lessons from a comprehensive review of oblique angle deposition-fabricated silver nanorod array substrates, Chem. Soc. Rev. 53 (2024) 1004, https://doi.org/10.1039/D3CS00540B.

[26] K. Muthumalai, N. Gokila, Y. Haldorai, R. Thangavelu, R. Kumar, Advanced wearable sensing technologies for sustainable precision agriculture – a review on chemical sensors, Adv. Sensor Res. 3 (2024) 2300107, https://doi.org/10.1002/ADSR.202300107.

[27] S.H. Shin, D.H. Kang, H.H. Yoon, J.Y. Park, M. Song, H. Son, D. Ha, H.J. Shin, 2D materials in logic technology: power efficiency and scalability in 2DM-MBC CFET, Nano Lett. 25 (2025) 7224–7233, https://doi.org/10.1021/ACS.NANOLETT.5C01061.

[28] C. Wang, Z. Wang, M. Gao, Y. Zhu, H. Zhu, L. Zhou, Y. Zhou, X. Tian, Y. Liu, Y. Zhang, S. Sun, C. Meng, X. Hong, Y. Wang, M. Yang, N. Fan, H. Huang, Z. Chen, Y. Ge, J. Li, K. Jiang, H. Zhang, M. Qiu, H. Wang, Highly stable and integrable graphene/molybdenum disulfide heterojunction field-effect transistor-based miRNA biosensor, ACS Appl. Mater. Interfaces 17 (2025) 28585–28596, https://doi.org/10.1021/ACSAMI.5C03827.

[29] J. Kim, S. Kwon, D.H. Cho, B. Kang, H. Kwon, Y. Kim, S.O. Park, G.Y. Jung, E. Shin, W.G. Kim, H. Lee, G.H. Ryu, M. Choi, T.H. Kim, J. Oh, S. Park, S.K. Kwak, S.W. Yoon, D. Byun, Z. Lee, C. Lee, Direct exfoliation and dispersion of two-dimensional materials in pure water via temperature control, Nat. Commun. (2015), https://doi.org/10.1038/NCOMMS9294;TECHMETA, 61. 6 (2015) 1–9.

[30] M.R. Azani, A. Hassanpour, T. Torres, Benefits, problems, and solutions of silver nanowire transparent conductive electrodes in indium tin oxide (ITO)-free flexible solar cells, Adv. Energy Mater. 10 (2020) 2002536, https://doi.org/10.1002/AENM.202002536;PAGE:STRING:ARTICLE/CHAPTER.

[33] R. Browning, P. Plachinda, R. Solanki, E.M. Bryant, D. Bayliss, P. Giannozzi, S. Baroni, N. Bonini, M. Calandra, R. Car, C. Cavazzoni, D. Ceresoli, G.L. Chiarotti, M. Cococcioni, I. Dabo, A. Dal Corso, S. De Gironcoli, S. Fabris, G. Fratesi, R. Gebauer, U. Gerstmann, C. Gougoussis, A. Kokalj, M. Lazzeri, L. Martin-Samos, N. Marzari, F. Mauri, R. Mazzarello, S. Paolini, A. Pasquarello, L. Paulatto, C. Sbraccia, S. Scandolo, G. Sclauzero, A.P. Seitsonen, A. Smogunov, P. Umari, R. M. Wentzcovitch, QUANTUM ESPRESSO: a modular and open-source software

project for quantum simulations of materials, J. Phys. Condens. Matter 21 (2009) 395502, https://doi.org/10.1088/0953-8984/21/39/395502/meta.

[34] T. Iqbal, M. Haqnawaz, M. Sultan, M.B. Tahir, M.I. Khan, K.N. Riaz, M. Ijaz, M. Rafique, Novel graphene-based transparent electrodes for perovskite solar cells, Int. J. Energy Res. 42 (2018) 4866, https://doi.org/10.1002/ER.4244.

[35] J.K. Jadoon, P.V. Pham, Hybrid TiO2–RGO nanocomposite as high specific capacitance electrode for supercapacitor, Nanotechnology 35 (2024) 435706, https://doi.org/10.1088/1361-6528/AD6A6A.

[36] S.V. Otari, M. Kumar, M.Z. Anwar, N.D. Thorat, S.K.S. Patel, D. Lee, J.H. Lee, J. K. Lee, Y.C. Kang, L. Zhang, Rapid synthesis and decoration of reduced graphene oxide with gold nanoparticles by thermostable peptides for memory device and photothermal applications, Sci. Rep. 7 (2017) 10980, https://doi.org/10.1038/S41598-017-10777-1;SUBJMETA.

[37] W. Zhang, H. Xu, F. Xie, X. Ma, B. Niu, M. Chen, H. Zhang, Y. Zhang, D. Long, General synthesis of ultrafine metal oxide/reduced graphene oxide nanocomposites for ultrahigh-flux nanofiltration membrane, Nat. Commun. 13 (2022) 471, https://doi.org/10.1038/S41467-022-28180-4;SUBJMETA.

[38] S. Liu, X. He, J. Zhu, L. Xu, J. Tong, Cu3P/RGO nanocomposite as a new anode for lithium-ion batteries, Sci. Rep. 6 (2016) 35189, https://doi.org/10.1038/SREP35189;TECHMETA.

[39] K. Dharmalingam, E. Thangavel, P.C. Tsai, P.V. Pham, K. Prakasham, G. Andaluri, K.B. Manjappa, Y.C. Lin, V.K. Ponnusamy, Novel MoS2-In2O3-WS2 (2D/3D/2D) ternary heterostructure nanocomposite material: efficient photocatalytic degradation of antimicrobial agents under visible-light, Environ. Res. 261 (2024) 119759, https://doi.org/10.1016/j.envres.2024.119759.

[40] R. Banu, N. Salvi, S. Gupta, C. Ameta, R. Ameta, P.B. Punjabi, A facile synthesis of GO/CuO nanocomposite with enhancing photocatalytic activity for the degradation of azure-B dye and its antimicrobial behavior, Arab. J. Sci. Eng. 47 (2022) 365–378, https://doi.org/10.1007/S13369-021-05421-0/METRICS.

[41] R. Mahdi, M. Alsultan, A. Al-Keisy, G.F. Swiegers, Photocatalytic hydrogen generation from pH-neutral water by a flexible tri-component composite, Catal. Lett. 151 (2021) 1700–1706, https://doi.org/10.1007/S10562-020-03427-1/METRICS.

[42] M. Liaqat, N.R. Khalid, T. Iqbal, I. Maryam, M. Tanveer, M.K. Hussain, P.V. Pham, A.M. Ali, M.A. Sayed, Synthesis of heterojunction BiVO4/MnO2 graphene ternary nanocomposites with enhanced photocatalytic activities through degradation of rhodamine B and tetracycline hydrochloride, Chin. J. Phys. 91 (2024) 406, https://doi.org/10.1016/j.cjph.2024.07.027.

[43] R. Ahmadi, R.F.N. Fatahi, P. Sangpour, M. Bagheri, T. Rahimi, Evaluation of antibacterial behavior of in situ grown CuO-GO nanocomposites, Mater. Today Commun. 28 (2021) 102642, https://doi.org/10.1016/j.mtcomm.2021.102642.

[44] E. Wu, K. Feng, R. Shi, R. Lv, F. Ouyang, S.S.C. Li, J. Zhong, J. Liu, Hybrid CuCoO–GO enables ultrasensitive detection of antibiotics with enhanced laser desorption/ionization at nano-interfaces, Chem. Sci. 10 (2018) 257–267, https://doi.org/10.1039/C8SC03692F.

[45] H. Chen, W. Ji, M. Gu, Y. Li, X. Cheng, Preparation and photocatalytic performance of CuO/GO heterojunction nanocomposite, J. Mater. Sci. Mater. Electron. 32 (2021) 27564–27575, https://link.springer.com/article/10.1007/s10854-021-07131-7 (accessed July 5, 2024), https://doi.org/10.1007/S10854-021-07131-7/METRICS.

[46] Y. Chen, S. Xia, W. Ren, Z. Zheng, J. Chen, K. Ma, C. Yu, X. Zhou, W. Zhang, A favorable improvement in reactivity between n-Al and sheet-like porous CuO as a nanoenergetic composite by graphene oxide additives, Ind. Eng. Chem. Res. 59 (2020) 12934, https://doi.org/10.1021/ACS.IECR.0C02138.

[47] D.B. Xiong, M. Cao, Q. Guo, Z. Tan, G. Fan, Z. Li, D. Zhang, High content reduced graphene oxide reinforced copper with a bioinspired nano-laminated structure and large recoverable deformation ability, Sci. Rep. 6 (2016) 33801, https://doi.org/10.1038/SREP33801;TECHMETA.

[48] M.F. Coelho, M.A. Rivas, G. Vilão, E.M. Nogueira, T.P. Iglesias, Permittivity and electrical conductivity of copper oxide nanofluid (12 nm) in water at different temperatures, J. Chem. Thermodyn. 132 (2019) 164–173, https://doi.org/10.1016/j.jct.2018.12.025.

[49] D.M. Tobaldi, K. Koci, M. Edelmannova, L. Lajaunie, B. Figueiredo, J.J. Calvino, M.P. Seabra, J.A. Labrincha, CuxO and carbon–modified TiO_2–based hybrid materials for photocatalytically assisted H2 generation, Mater. Today Energy. 19 (2021) 100607, https://doi.org/10.1016/j.mtener.2020.100607.

[50] K. Kala, V. Vasumathi, S. Sivalingam, B.S.C. Kapali, Optimization of organic dyes photodegradation and investigation of the anticancer performance by copper oxide/graphene oxide nanocomposite, Surf. Interfaces 50 (2024) 104482, https://doi.org/10.1016/j.surfin.2024.104482.

[51] P. Phogat, Shreya, R. Jha, S. Singh, Synthesis of novel ZnO nanoparticles with optimized band gap of 1.4 eV for high-sensitivity photo electrochemical detection, Mater. Today Sustain. 27 (2024) 100823, https://doi.org/10.1016/j.mtsust.2024.100823.

[52] J. Samuel, A. Shah, D. Kumar, L. Robindro Singh, M. Mahato, Preparation, characterization and some electrochemical study of waste derived iron oxide-carbon nanocomposite, Mater. Today Proc. 47 (2021) 1048, https://doi.org/10.1016/j.matpr.2021.06.239.

[53] I. Altin, CuO-TiO2/graphene ternary nanocomposite for highly efficient visible-light-driven photocatalytic degradation of bisphenol A, J. Mol. Struct. 1252 (2022) 132199, https://doi.org/10.1016/j.molstruc.2021.132199.

[54] M. Yousaf, R.M. Munir, T. Iqbal, S. Afsheen, M.I. Khan, H. Wali, H.I. Rizvi, P. V. Pham, A.A. AlObaid, I. Warad, S. Rafique, Exploring innovative antibacterial properties of porous ALT (Al_2O_3/TiO_2) composite, Mater. Chem. Phys. 325 (2024) 129736, https://doi.org/10.1016/j.matchemphys.2024.129736.

[55] G.M. Lohar, O.C. Pore, A.V. Fulari, Electrochemical behavior of CuO/rGO nanopellets for flexible supercapacitor, non-enzymatic glucose, and H_2O_2 sensing application, Ceram. Int. 47 (2021) 16674–16687, https://doi.org/10.1016/j.ceramint.2021.02.238.

[56] G.A. Sundaram, S. Kumaravelu, W.L. Tseng, P.V. Pham, A.S.K. Kumar, V. Parimelazhagan, Fine-tuned graphene oxide nanocomposite: harnessing copper(II)–imidazole complex for enhanced biological responses and balanced photocatalytic functionality, Materials (Basel) 17 (2024) 892, https://doi.org/10.3390/ma17040892.

[57] H. Long, R. Huang, X. Liu, C. Chen, Preparation and photocatalytic performance of ZnO/CuO/GO heterojunction under visible light, Inorg. Chem. Commun. 136 (2022) 109097, https://doi.org/10.1016/j.inoche.2021.109097.

[58] V. Vasilopoulos, M. Pitou, I. Fekas, R. Papi, A. Ouranidis, E. Pavlidou, P. Patsalas, Graphene-wrapped copper nanoparticles: an antimicrobial and biocompatible nanomaterial with valuable properties for medical uses, ACS Omega 5 (2020) 26329–26334, https://doi.org/10.1021/ACSOMEGA.0C00834.

[59] P.V. Pham, T.H. Mai, S.P. Dash, V. Biju, Y.L. Chueh, D. Jariwala, V. Tung, Transfer of 2D films: from imperfection to perfection, ACS Nano 18 (2024) 14841–14876, https://doi.org/10.1021/ACSNANO.4C00590.

[60] R. Wang, Y. Xu, C. Wang, H. Zhao, R. Wang, X. Liao, L. Chen, G. Chen, Fabrication of ITO-rGO/Ag NPs nanocomposite by two-step chronoamperometry electrodeposition and its characterization as SERS substrate, Appl. Surf. Sci. 349 (2015) 805–810, https://doi.org/10.1016/j.apsusc.2015.05.067.

[61] A. Qadir, T.K. Le, M. Malik, K.A. Amedome Min-Dianey, I. Saeed, Y. Yu, J.R. Choi, P.V. Pham, Representative 2D-material-based nanocomposites and their emerging applications: a review, RSC Adv. 11 (2021) 23860, https://doi.org/10.1039/D1RA03425A.

[62] T.J. Quill, G. Lecroy, D.M. Halat, R. Sheelamanthula, A. Marks, L.S. Grundy, I. Mcculloch, J.A. Reimer, N.P. Balsara, A. Giovannitti, A. Salleo, C.J. Takacs, An ordered, self-assembled nanocomposite with efficient electronic and ionic transport, Nat. Mater. 22 (2023) 362–368, https://doi.org/10.1038/S41563-023-01476-6;TECHMETA.

[63] F.K. Algethami, H.M. Marwani, N. Raza, A.M. Asiri, M.M. Rahman, Non-enzymatic electrochemical detection of melamine in dairy products by using CuO decorated carbon nanotubes nanocomposites, Food Chem. 445 (2024) 138792, https://doi.org/10.1016/j.foodchem.2024.138792.

[64] E.S. Ganya, N. Soin, S.J. Moloi, J.A. McLaughlin, W.F. Pong, S.C. Ray, Polyacrylate grafted graphene oxide nanocomposites for biomedical applications, J. Appl. Phys. 127 (2020) 054302, https://doi.org/10.1063/1.5135572.

[65] S. Santhoshkumar, E. Murugan, Rationally designed SERS AgNPs/GO/g-CN nanohybrids to detect methylene blue and Hg2+ ions in aqueous solution, Appl. Surf. Sci. 553 (2021) 149544, https://doi.org/10.1016/j.apsusc.2021.149544.

[66] S. Santhoshkumar, S.W. Wei, C.C. Kuo, M. Madhu, A. Santhana Krishna Kumar, W. Bin Tseng, C.Y. Lu, W.L. Tseng, Engineering of phase composition in molybdenum disulfide nanoflowers to amplify SERS activity: sensitivity enhancement through dispersive liquid-liquid microextraction integration, Sensors Actuators B Chem. 422 (2025) 136577, https://doi.org/10.1016/j.snb.2024.136577.

[67] D. Yu, L. Xu, H. Zhang, J. Li, W. Wang, L. Yang, X. Jiang, B. Zhao, A new semiconductor-based SERS substrate with enhanced charge collection and improved carrier separation: CuO/TiO2 p-n heterojunction, Chin. Chem. Lett. 34 (2023) 107771, https://doi.org/10.1016/j.cclet.2022.107771.

[68] K. Xu, H. Yan, C.F. Tan, Y. Lu, Y. Li, G.W. Ho, R. Ji, M. Hong, Hedgehog inspired CuO nanowires/Cu2O composites for broadband visible-light-driven recyclable surface enhanced Raman scattering, Adv. Opt. Mater. 6 (2018) 1701167, https://doi.org/10.1002/adom.201701167.

[69] S. Sharma, R. Kumar, R.M. Yadav, Polyacrylonitrile/N-doped graphene quantum dots nanocomposite activity as SERS nanosensors for detection of methylene blue, Mater. Today Commun. 36 (2023) 106860, https://doi.org/10.1016/j.mtcomm.2023.106860.

[70] Y. Guan, M. Chen, Y. Ding, Y. Fang, F. Huang, C.Y. Xu, L. Zhen, Y. Li, L. Yang, P. Xu, Phase transformation on multilayer 2M-WS2 for improved surface-enhanced Raman scattering, ACS Nano 18 (2024) 17339–17348, https://doi.org/10.1021/ACSNANO.4C06303.

[71] Z. Zhuang, J. Wang, J. Huang, R. Hong, C. Tao, Q. Wang, H. Lin, Z. Han, D. Zhang, S. Zhuang, Fabrication of high-stability and -sensitivity perovskite nanoparticles with a core-shell structure for surface-enhanced Raman scattering, J. Phys. Chem. C 128 (2024) 10120–10132, https://doi.org/10.1021/ACS.JPCC.4C00841.

[72] G. Kim, D.W. Jeong, G. Lee, S. Lee, K.Y. Ma, H. Hwang, S. Jang, J. Hong, S. Pak, S. N. Cha, D. Cho, S. Kim, J. Lim, Y.W. Lee, H.S. Shin, A.R. Jang, J.O. Lee, Unusual Raman enhancement effect of ultrathin copper sulfide, Small 20 (2024) 2306819, https://doi.org/10.1002/smll.202306819.

[73] S. Majumder, B. Satpati, S. Kumar, S. Banerjee, Multifunctional reduced graphene oxide wrapped circular Au nanoplatelets: enhanced photoluminescence, excellent surface-enhanced Raman scattering, photocatalytic water splitting, and non-enzymatic biosensor, ACS Appl. Nano Mater. 1 (2018) 3945–3955, https://doi.org/10.1021/ACSANM.8B00730.

[74] S. Sheng, Y. Ren, S. Yang, Q. Wang, P. Sheng, X. Zhang, Y. Liu, Remarkable SERS detection by hybrid Cu2O/Ag nanospheres, ACS Omega 5 (2020) 17703–17714, https://doi.org/10.1021/ACSOMEGA.0C02301.

[75] S. Jiang, Y. Zhang, R. Zhang, C. Hu, M. Liao, Y. Luo, J. Yang, Z. Dong, J.G. Hou, Distinguishing adjacent molecules on a surface using plasmon-enhanced Raman scattering, Nat. Nanotechnol. 10 (2015) 865–869, https://doi.org/10.1038/NNANO.2015.170;TECHMETA.

[76] G. Li, W. Bin Gong, T. Qiu, S. Cong, Z. Zhao, R. Ma, Y. Michiue, T. Sasaki, F. Geng, Surface-modified two-dimensional titanium carbide sheets for intrinsic vibrational signal-retained surface-enhanced Raman scattering with ultrahigh uniformity, ACS Appl. Mater. Interfaces 12 (2020) 23523–23531, https://doi.org/10.1021/ACSAMI.0C00908.

[77] L. Chen, H.L. Hou, M. Prato, Fabrication of covalently bonded MoS2–graphene heterostructures with different organic linkers, Commun. Mater. 5 (2024) 1–9, https://doi.org/10.1038/S43246-024-00571-8;SUBJMETA.

[78] D. Liu, X. Chen, Y. Hu, T. Sun, Z. Song, Y. Zheng, Y. Cao, Z. Cai, M. Cao, L. Peng, Y. Huang, L. Du, W. Yang, G. Chen, D. Wei, A.T.S. Wee, D. Wei, Raman enhancement on ultra-clean graphene quantum dots produced by quasi-equilibrium plasma-enhanced chemical vapor deposition, Nat. Commun. 9 (2018) 1–10, https://doi.org/10.1038/s4146701702627-5.

[79] S. Guo, S. Jin, E. Park, L. Chen, L. Guo, Y.M. Jung, Enhanced surface-enhanced Raman scattering activity of MoS2-Ag-reduced graphene oxide: structure-mediated excitonic transition, J. Phys. Chem. C 125 (2021) 23259–23266, https://doi.org/10.1021/ACS.JPCC.1C06387.

[80] Q. Shao, X. Zhang, P. Liang, Q. Chen, X. Qi, M. Zou, Fabrication of magnetic Au/Fe3O4/MIL-101(Cr) (AF-MIL) as sensitive surface-enhanced Raman spectroscopy (SERS) platform for trace detection of antibiotics residue, Appl. Surf. Sci. 596 (2022) 153550, https://doi.org/10.1016/j.apsusc.2022.153550.

[81] J.E.S. van der Hoeven, H. Gurunarayanan, M. Bransen, D.A.M. de Winter, P.E. de Jongh, A. van Blaaderen, Silica-coated gold nanorod supraparticles: a tunable platform for surface enhanced Raman spectroscopy, Adv. Funct. Mater. 32 (2022) 2200148, https://doi.org/10.1002/adfm.202200148.

[82] W. Liu, Z. Wang, X. Tang, Z. Liu, Y. Xiong, X. Zhou, G. Zhu, Z. Zhao, W. Yan, L. Shi, L. Huang, Y. Liu, S. Cui, X. He, Construction of ultrasensitive surface-enhanced Raman scattering substates based on TiO2 aerogels, Adv. Opt. Mater. 11 (2023) 2300730, https://doi.org/10.1002/adom.202300730.

[83] Q. Zhang, X. Li, Q. Ma, Q. Zhang, H. Bai, W. Yi, J. Liu, J. Han, G. Xi, A metallic molybdenum dioxide with high stability for surface enhanced Raman spectroscopy, Nat. Commun. 8 (2017) 1–9, https://doi.org/10.1038/NCOMMS14903;TECHMETA.

[84] M. Yilmaz, E. Babur, M. Ozdemir, R.L. Gieseking, Y. Dede, U. Tamer, G.C. Schatz, A. Facchetti, H. Usta, G. Demirel, Nanostructured organic semiconductor films for molecular detection with surface-enhanced Raman spectroscopy, Nat. Mater. 16 (2017) 918–924, https://doi.org/10.1038/NMAT4957;TECHMETA.

[85] W. Shan, R. Liu, H. Zhao, Z. He, Y. Lai, S. Li, G. He, J. Liu, In situ surface-enhanced Raman spectroscopic evidence on the origin of selectivity in CO2 electrocatalytic reduction, ACS Nano 14 (2020) 11363–11372, https://doi.org/10.1021/acsnano.0c03534.

[86] B. Arumugam, V. Nagarajan, J. Annaraj, S.K. Ramaraj, Barium titanate nanoparticle-based disposable sensor for nanomolar level detection of the haematotoxic pollutant quinol in aquatic systems, New J. Chem. 46 (2022) 3006–3016, https://doi.org/10.1039/D1NJ04807D.

[87] N. Karikalan, R. Karthik, S.M. Chen, M. Velmurugan, C. Karuppiah, Electrochemical properties of the acetaminophen on the screen printed carbon electrode towards the high performance practical sensor applications, J. Colloid Interface Sci. 483 (2016) 109–117, https://doi.org/10.1016/j.jcis.2016.08.028.

[88] N.A. Rajpurohit, H. Agrawal, K. Bhakar, K. Panchal, D. Kumar, A stable and efficient electrochemical sensor for hydroquinone and catechol detection in real-world water samples using mesoporous CaM@rGO nanocomposite, Sens. Actuators B 420 (2024) 136481, https://doi.org/10.1016/j.snb.2024.136481.

[89] S. Radhakrishnan, K. Krishnamoorthy, C. Sekar, J. Wilson, S.J. Kim, A promising electrochemical sensing platform based on ternary composite of polyaniline–Fe2O3–reduced graphene oxide for sensitive hydroquinone determination, Chem. Eng. J. 259 (2015) 594–602, https://doi.org/10.1016/j.cej.2014.08.047.

[90] X. Yuan, Y. Jin, J. Guo, Q. Wang, L. Xu, Y. Song, X. Xiong, Cu single atoms embedded in N-doped hollow carbon spheres for simultaneous electrochemical detection of hydroquinone and catechol, ACS Appl. Nano Mater. 7 (2024) 14154–14163, https://doi.org/10.1021/acsanm.4c01686.

[91] N. Li, J.R. Huang, H.Y. Zhang, M. Cui, B. Sun, C. Zhang, H.Y. Zhao, Decoration of covalent Polyoxometalate-organic frameworks with Pt nanoparticles and multiwalled carbon nanotubes for simultaneous electrochemical detection of hydroquinone and catechol, ACS Appl. Nano Mater. 7 (2024) 1960–1969, https://doi.org/10.1021/acsanm.3c05232.

[92] T. Zhang, J.Z. Wei, X.J. Sun, X.J. Zhao, H.L. Tang, H. Yan, F.M. Zhang, Continuous and rapid synthesis of UiO-67 by electrochemical methods for the electrochemical detection of hydroquinone, Inorg. Chem. 59 (2020) 8827–8835, https://doi.org/10.1021/acs.inorgchem.0c00580.

[93] J.N. Tiwari, V. Vij, K.C. Kemp, K.S. Kim, Engineered carbon-nanomaterial-based electrochemical sensors for biomolecules, ACS Nano 10 (2016) 46–80, https://doi.org/10.1021/acsnano.5b05690.

[94] R. Murugan, K.Y. Hwa, A. Santhan, 2D-graphitic carbon nitride nanosheet/metal nanocomposites for electrochemical sensors of hydroquinone in real sample analysis, ACS Appl. Nano Mater. 6 (2023) 8550–8563, https://doi.org/10.1021/acsanm.3c00877.

[95] D.C. Patra, S.P. Mondal, Paper-based electrochemical sensor integrated with gold nanoparticle-decorated carbon cloth as a working electrode for nitric oxide detection in artificial tears, ACS Appl. Bio Mater. 7 (2024) 5247–5257, https://doi.org/10.1021/acsabm.4c00425.

[96] H. Zhu, Y. Fu, F. Meng, X. Wu, Z. Gong, Q. Ding, M.V. Gustafsson, M.T. Trinh, S. Jin, X.Y. Zhu, Lead halide perovskite nanowire lasers with low lasing thresholds and high quality factors, Nat. Mater. (2014), https://doi.org/10.1038/NMAT4271;TECHMETA, 146. 14 (2015) 636–642.

[97] B. Schuler, S. Fatayer, F. Mohn, N. Moll, N. Pavlieèk, G. Meyer, D. Penã, L. Gross, Reversible Bergman cyclization by atomic manipulation, Nat. Chem. 83 (2016) 220–224, https://doi.org/10.1038/NCHEM.2438;TECHMETA, 8 (2016).

[98] J.N. Baby, B. Akila, T.W. Chiu, S. Sakthinathan, V. Abhikha Sherlin, A. Zealma B, M. George, Deep eutectic solvent-assisted synthesis of a strontium tungstate bifunctional catalyst: investigation on the electrocatalytic determination and photocatalytic degradation of acetaminophen and metformin drugs, Inorg. Chem. 62 (2023) 8249–8260, https://doi.org/10.1021/acs.inorgchem.3c00676.

[99] A.U. Alam, Y. Qin, M. Catalano, L. Wang, M.J. Kim, M.M.R. Howlader, N.X. Hu, M.J. Deen, Tailoring MWCNTs and β-cyclodextrin for sensitive detection of acetaminophen and estrogen, ACS Appl. Mater. Interfaces 10 (2018) 21411–21427, https://doi.org/10.1021/acsami.8b04639.

[100] H. Gu, X. Shui, Y. Zhang, T. Zeng, J. Yang, Z. Wu, X. Zhang, N. Yang, Porous carbon scaffolded Fe-based alloy nanoparticles for electrochemical quantification of acetaminophen and rutin, Carbon N. Y. 221 (2024) 118954, https://doi.org/10.1016/j.carbon.2024.118954.

[101] Y. Zhang, E. Gao, V.P. Fedin, Molybdenum disulfide-filled double-sandwiched Cd-MOF for the quantitative detection of nanomolar acetaminophen and dopamine in pharmaceuticals, Chem. Eng. J. 498 (2024) 155469, https://doi.org/10.1016/j.cej.2024.155469.

[102] M.H. Afzal, W. Pervaiz, Z. Huang, Z. Wang, G. Li, H. Liu, In situ synthesis of a UIO-66-NH 2 @Ti 3 C 2 composite for advanced electrochemical detection of acetaminophen, Nanoscale 17 (2025) 4444–4454, https://doi.org/10.1039/D4NR04388J.

[103] A. Mader, U. Riehle, T. Brandstetter, E. Stickeler, J. Ruehe, Universal nucleic acid sequence-based amplification for simultaneous amplification of messengerRNAs and microRNAs, Anal. Chim. Acta 754 (2012) 1–7, https://doi.org/10.1016/j.aca.2012.09.045.

[104] R. Li, H. Qi, Y. Ma, Y. Deng, S. Liu, Y. Jie, J. Jing, J. He, X. Zhang, L. Wheatley, C. Huang, X. Sheng, M. Zhang, L. Yin, A flexible and physically transient electrochemical sensor for real-time wireless nitric oxide monitoring, Nat. Commun. 11 (2020) 1–11, https://doi.org/10.1038/S41467-020-17008-8;TECHMETA.

[105] B.G. Mahmoud, M. Khairy, F.A. Rashwan, C.E. Banks, Simultaneous voltammetric determination of acetaminophen and isoniazid (hepatotoxicity-related drugs) utilizing bismuth oxide nanorod modified screen-printed electrochemical sensing platforms, Anal. Chem. 89 (2017) 2170–2178, https://doi.org/10.1021/ACS.ANALCHEM.6B05130.

[106] H. Karimi-Maleh, Z. Zhang, N. Zare, O. Karaman, Y. Wen, T. Wu, N. Zhong, L. Fu, A novel disposable dual-sensing platform based on DNA-aptamer amplified with gold nanoparticles/Nb4C3-MXene for simultaneous detection of lead and cadmium, Adv. Compos. Hybrid Mater. 8 (2025) 1–11, https://doi.org/10.1007/S42114-025-01216-1/TABLES/1.

[107] Y. Gao, T. Chu, C. Zhou, W. Huang, Y. Zheng, Fe, Cu co-doped carbon nanosheets for electrochemical-colorimetric detection of acetaminophen, ACS Appl. Nano Mater. 7 (2024) 14321–14330, https://doi.org/10.1021/ACSANM.4C01798.

[108] P.E. Blochl, Projector augmented-wave method, Phys. Rev. B 50 (1994) 17953–17979, https://doi.org/10.1103/PhysRevB.50.17953.

[109] J.P. Perdew, K. Burke, M. Ernzerhof, Generalized gradient approximation made simple, Phys. Rev. Lett. 77 (1996) 3865–3868, https://doi.org/10.1103/PhysRevLett.77.3865.

[110] S. Grimme, J. Antony, S. Ehrlich, H. Krieg, A consistent and accurate ab initio parametrization of density functional dispersion correction (DFT-D) for the 94 elements H-Pu, J. Chem. Phys. 132 (2010) 154104, https://doi.org/10.1063/1.3382344.